

## High-resolution reconstructions of Holocene Sea-surface conditions from dinoflagellate cyst assemblages in the northern South China Sea

Li Zhen <sup>1,2,\*</sup>, Pospelova Vera <sup>2,3</sup>, Liu Lejun <sup>4</sup>, Francois Roger <sup>1</sup>, Wu Yongsheng <sup>5</sup>, Mertens Kenneth <sup>6</sup>, Saito Yoshiki <sup>7,8</sup>, Zhou Rui <sup>9</sup>, Song Bing <sup>10</sup>, Xie Xin <sup>11</sup>

<sup>1</sup> Department of Earth, Ocean and Atmospheric Sciences, University of British Columbia, 329 West Mall, Vancouver, British Columbia V6T 1Z4, Canada

<sup>2</sup> School of Earth and Ocean Sciences, University of Victoria, PO Box 1700 STN CSC, Victoria, British Columbia V8W 2Y2, Canada

<sup>3</sup> Department of Earth and Environmental Sciences, University of Minnesota, 116 Church St SE, Minneapolis, MN 55455, USA

<sup>4</sup> First Institute of Oceanography, MNR, 6 Xianxialing Road, Qingdao 266061, China

<sup>5</sup> Fisheries and Oceans Canada, Bedford Institute of Oceanography, Dartmouth, Nova Scotia B2Y 4A2, Canada

<sup>6</sup> Ifremer, LER BO, Station de Biologie Marine, Place de la Croix, BP40537, F-29185 Concarneau Cedex, France

<sup>7</sup> Estuary Research Center, Shimane University, Nishikawatsu-cho 1060, Matsue 690-8504, Japan

<sup>8</sup> Geological Survey of Japan, AIST, Tsukuba 305-8567, Japan

<sup>9</sup> State Key Laboratory of Estuarine and Coastal Research, East China Normal University, Shanghai, China

<sup>10</sup> Nanjing Institute of Geography and Limnology, Chinese Academy of Sciences, 73 East Beijing Road, Nanjing 210008, China

<sup>11</sup> State Key Laboratory of Marine Geology, Tongji University, 1239 Siping Road, Shanghai 20092, China

\* Corresponding author : Zhen Li, email address : [zhenli@eoas.ubc.ca](mailto:zhenli@eoas.ubc.ca)

### Abstract :

A high-resolution dinoflagellate cyst analysis on a sediment core GLW1D from the northern South China Sea (SCS) was performed to reconstruct paleoceanographic conditions over the last 12,500 years through qualitative, semi-quantitative, and quantitative methods. A modern dataset with 398 reference sites in the northern Pacific was assembled and used to identify the relationship between dinoflagellate cyst assemblages and sea-surface temperature (SST), sea-surface salinity (SSS) and primary productivity (PP). Modern analog technique (MAT) was applied to offer first dinoflagellate-cyst-based quantitative estimates of Holocene sea-surface conditions in the western North Pacific. The downcore reconstructions show that SST, SSS and PP were predominantly controlled by the changes in coastal and oceanic currents due to the changes of sea level and monsoon systems. Our results indicate that SST increased while SSS and PP decreased from 12,500 to ~6800 cal yr BP, reaching the maximum SST and the minimum SSS and PP during ~6800–5000 cal yr BP, and followed by a slight decline in SST with minor increases in SSS and PP. The three intervals correspond to the regional onshore sea-level stages of

---

rising, stabilization in a highstand and slight drop, respectively. The Kuroshio Current strongly influenced the core site before ~9900 cal yr BP, reflected by the highest abundances of oceanic *Impagidinium* spp. and high reconstructed SSS values. This can be explained by a lack of water input from the East China Sea before the opening of the Taiwan Strait. The warmest period, from ~6800 cal yr BP to ~5500 cal yr BP, is recorded by the highest *Dapsilidinium pastielsii* abundances. Two short-term high-PP events of ~2700–2400 cal yr BP and ~1000–600 cal yr BP, which were characterized by opposite climatic conditions, coincided with two notable societal (dynasty) collapses of China. Enhanced anthropogenic activities since the Late Bronze Age most likely partially affected the high PP through influencing river inputs to the northern SCS.

### Highlights

► It contributes the first dinocyst-based quantitative reconstruction in the western Pacific. ► Taiwan Strait might open at ~9900 cal yr BP, showed by a decrease in *Impagidinium*. ► The warmest water in the northern South China Sea was in ~6800–5500 cal yr BP. ► A cold event at ~2700–2400 cal yr BP was identified. ► Human activities partially contributed to the high PP events in the late Holocene.

**Keywords** : Paleoceanography, Sea-surface temperature, Sea-surface salinity, Marine primary productivity, Dinoflagellate cysts, the South China Sea, Holocene, Anthropogenic impacts

## 1. Introduction

The South China Sea (SCS), located in the low-latitude western Pacific and the East Asian climate region, is a prime region for studying both climate variability and ocean currents. Since the Last Glacial Maximum (LGM), climate warming and sea-level rise have caused changes in oceanographic conditions of the SCS (e.g., Wei et al., 1997; Yim and Huang, 2002; Zhao and Yu, 2002; Liu et al., 2013; Li et al., 2017; Xiong et al., 2018b; Xia et al., 2019; Zhou et al., 2019). With the sea-level rise, the paleo-shoreline migrated landward, some water channels were opened and allowed water exchanges between different seas. For example, the Taiwan Strait formation enabled water exchange between the SCS and the East China Sea (ECS) (e.g., Li et al., 2017), and the formation of Taiwan Warm Current (Hsieh and Saito, 2017) and changes in strength of the Kuroshio Current intrusion (e.g., Ujike et al., 2003; Liu et al., 2013) influenced the circulation in the SCS. Such hydrographic and environmental changes influence marine ecosystem compositions and structure, which can be recorded in sediments. The northern SCS is considered a prime area for reconstructing high-resolution Holocene climatic and oceanographic variability due to its well-preserved sedimentary strata and relatively high sedimentation rates. A number of studies have analyzed sediment cores from the northern SCS to reconstruct the climatic variability and hydrographic conditions of the Holocene, including sea-surface temperature (SST) and sea surface salinity (SSS) (e.g., Huang et al., 1997; Wang et al., 1999; Yu et al., 2005; He et al., 2008; Huang et al., 2009; Dai and Weng, 2015; Li et al., 2017). Wang et al. (1999) reported a high-amplitude perturbation in monsoon moisture around 8150 cal yr BP and Holocene periodicities of 84, 102 and near 775 yr in monsoon variation in the South China Sea using oxygen isotopes. Using diatoms, Huang et al. (2009) distinguished the Holocene Climate Optimum and three Holocene cooling events. They also reported a strong coastal water influence

on the slope of northern South China Sea during the interval 11,150–8050 cal. yr BP, reflected by an increase in the abundance of coastal diatom species. Dai and Weng (2015) reported a notably enhanced terrestrial runoff and precipitation during ~11,300–9400 cal yr BP and a gradually warming climate thereafter based on pollen records. Li et al. (2017) identified the opening time of the Strait of Taiwan, the Holocene Optimum, and three strengthened winter monsoon intervals at ~5500 cal yr BP, 4000 cal yr BP, and 2500 cal yr BP through records of pollen, spores and dinoflagellate cysts.

Quantitative reconstructions across the northern SCS have incorporated various paleoclimatic proxies, including Sr/Ca ratios of *Tridacna gigas* shells (e.g., Yan et al., 2015), coralline Sr/Ca ratios (e.g., Wei et al., 2007), foraminiferal Mg/Ca ratios (e.g., Steinke et al., 2011), alkenone abundances (e.g., Wu et al., 2017) and foraminifera (e.g., Lin et al., 2006; Contreras-Rosales et al., 2019), and diatom assemblages (e.g., Jiang et al., 2014). These reconstructions inferred a more stable Holocene climate comparing to that of the late Pleistocene/Holocene transition. However, many of these studies showed contrasting results in the Holocene, with reconstruction resolution being one of the reasons. The annual-resolution estimates of SST can reflect more detailed information on climate fluctuations, but only a few studies provide such resolution and only for a very specific period. For example, Wei et al. (2006) studied annual and seasonal Sr/Ca ratios in corals spanning from 6100 to 6500 cal yr BP and estimated winter, summer and annual SSTs in this period were 0.5–1.4°C, 0–2.0°C, and 0.2–1.5°C higher than the present, respectively. Comparatively, centennial or millennial-scale estimates display long-term variations of the SST. For example, Wu et al. (2017) reconstructed coastal SST based-on alkenone unsaturation ratios and found that SST increased from 23.0°C at ~10,350 cal yr BP to the peak of ~27.7°C at 8900-8700 cal yr BP, then, kept relatively stable

thereafter except for several centennial cooling events. In contrast, foraminifer-based millennial-scale estimates of SST and SSS in a slope region showed that the highest SST of  $\sim 27^{\circ}\text{C}$  occurred after  $\sim 6000$  cal yr BP (Lin et al., 2006). Kong et al. (2014) reported a difference in two estimates of SST over the past 8000 yr in nearshore and offshore of the Pear River region by using a long-chain alkenone unsaturation. Even when different proxies were used on the same sediment core, higher-resolution events of paleo-monsoon climate record or paleoceanographic parameters were variable. For example, different SSSs were reconstructed by diatoms (Jiang et al., 2014) and by  $\delta^{18}\text{O}$  of foraminifera (Wang et al., 1999) from core 17940 from the north SCS. Therefore, the discrepancies in the quantitative reconstructions may be due to differences in site locations, sediment sources, sampling resolution (time scales) or limitations of individual proxies associated with local oceanographic conditions such as the relative sea level (RSL) and currents.

Terrestrial sediments in the northern SCS are sourced from numerous regions, including the Luzon Island, South China and Taiwan (see Fig. 1) (e.g., Liu et al., 2016). The river-borne and monsoon-carried material from these sources is distributed differently in the SCS and is influenced by wind direction and strength, rivers, currents and geomorphological patterns. Sediments from Taiwan are primarily transported to the deep basin of the SCS (e.g., Ludmann et al., 2005; Shao et al., 2007). Materials from the Pearl River are transported southwestward along the coast and deposited on the shelf between the Pearl River estuary and Hainan Island (e.g., Liu et al., 2013a). Sediments from Luzon are typically deposited northwest of Luzon Island (e.g., Liu et al., 2011). As a result, the sediment sourced to the continental slope is highly variable, affected by both riverine inputs and currents. Compared to the upper slope, the middle or lower continental slope of the northern SCS are mostly influenced by turbidity and/or bottom currents (e.g., Zhao et al., 2015). For example, the Dongsha and Zhujiang sections on the slope have

high-sedimentary accumulation rates because of high input of terrestrial materials. The sediments in the Dongsha section transported by bottom currents form high-sedimentation-rate drifts (Ludmann et al., 2005; Shao et al., 2007), and ~40% of the terrestrial material is derived from the Luzon region (Liu et al., 2008). In contrast, the Pearl River from South China and numerous rivers from southwest Taiwan transport the majority of the terrestrial material to the Zhujiang (Pearl River) slope, while less terrestrial material is derived from Luzon Island (Liu et al., 2008).

On the other hand, Holocene relative sea-level (RSL) rise greatly changed sediment sources and oceanographic conditions in the SCS (e.g., changes in local currents and water masses). The RSL curves of the SCS (based on mangrove peat, corals, oyster beds, tubeworms, and beach rock exposures or other intertidal deposits) show a ~60 m rise in sea level from the Younger Dryas/Holocene transition to ~7–6 cal kyr BP (e.g., Hanebuth et al., 2000; Liu et al., 2004; Zong, 2004; Tanabe et al., 2006). Caused by the general RSL rise, the shorelines of the SCS migrated landward and terrestrial input was reduced due to the increased proximity to the terrestrial sources. Sediment delivery to the SCS has also been unstable since the LGM. The Pearl River sediment supply peaked during the LGM, whereas the sediment contribution from Taiwan was relatively low (Liu et al., 2015). When the sea-level rise during the deglaciation, the relative contribution of Taiwan-derived materials increased in the northern continental slope, while the Pearl River contribution gradually decreased (e.g., Liu et al., 2016). In addition, the Taiwan Strait opening at the beginning of the Holocene (e.g., Li et al., 2017) and the Taiwan Warm Current formation during the mid-Holocene (e.g., Hsiung and Saito, 2017) have altered the general oceanographic currents in the northern SCS. Therefore, a comparison of multi-proxy paleoceanographic datasets across different geomorphological units in the SCS can help to reveal

past changes in regional sea-surface conditions, including the responses of SST, SSS, and primary productivity (PP) to specific regional climatic and oceanographic events.

Microfossils such as planktonic foraminifera (e.g., Imbrie and Kipp 1971), radiolarians (e.g., Geitzenauer et al., 1976), and diatoms (e.g., Maynard, 1976) are commonly used to quantitatively reconstruct past SST, SSS and PP. However, these calcareous and siliceous microfossils are prone to dissolution which can bias results. Dinoflagellates are important primary producers and many species produce cysts during their life cycle. These cysts can be well preserved in sediments, as they are resistant to physical, chemical and biological degradation (e.g., Dale, 1996). The spatial distribution of dinoflagellate cysts has been widely documented (e.g., Wall et al., 1977; Harland, 1983; Dogue and Harland, 1991; Zonneveld, 1997; Rochon et al., 1999; Mudie and Rochon, 2001; Marret and Zonneveld, 2003; de Vernal et al., 2001, 2013, 2020; Pospelova et al., 2004, 2005; Radi and de Vernal, 2004; Limoges et al., 2010; Verleye and Louwye, 2010; Verleye et al., 2011; Richerol et al., 2012; Zonneveld et al., 2013; Heikkilä et al., 2014; Price et al., 2015; Mudie et al., 2017; Gurdebeke et al., 2018; Li et al., 2020). Assemblages of dinoflagellate cysts are robust to be climatic, oceanographic, and/or ecological indicators of past oceanographic conditions (e.g., Harland, 1973; Meon and Pannetier, 1994; Harland and Howe, 1995; Zonneveld, 1996; Zonneveld et al., 1997, 2008; Marret et al., 2001, 2019; Pospelova et al., 2002, 2006, 2015; Reichert and Brinkhuis, 2003; Richerol et al., 2008; Londeix et al., 2009; Mertens et al., 2009; Price et al., 2013; Bringué et al., 2014; Limoges et al., 2014; Richerol et al., 2014; Narale et al., 2015; Harland et al., 2016; Richerol et al., 2016; Li et al., 2017; Zhao et al., 2019). A surface sediment dinoflagellate cyst database from various marine environments has also been used for quantitative reconstructions, including past winter and summer SST, SSS, sea-ice cover, and PP (e.g., de Vernal et al., 1994, 1997, 2001, 2013,

2020; Rochon et al., 1998; Mudie et al., 2001; Solignac et al., 2006; Ledu et al., 2008, 2010; Radi and de Vernal, 2008b; Verleye et al., 2009; Mertens et al., 2012; Pospelova et al., 2015; Van Nieuwenhove et al., 2018; Caron et al., 2019; Datema et al., 2019). However, most of these reconstructions were conducted in the Atlantic and high-latitude regions, whereas few studies focused on the low-latitude areas of the Pacific because of a lack of reference datasets of dinoflagellate cysts for this region. Fortunately, a recent surface sediment dinoflagellate cyst dataset across the SCS (Li et al., 2020) has been established, and it can be added to the northern Pacific dinoflagellate cyst dataset (de Vernal et al., 2020) (Fig. 1). The combined data should provide information on the relationship between dinoflagellate cyst assemblages and oceanographic parameters to achieve quantitative paleoceanographic reconstructions in the northern SCS. Dinoflagellate cyst assemblages and a high-resolution pollen record from a sediment core in the northern SCS were analyzed to reconstruct the Holocene monsoon climate and oceanographic conditions (Li et al., 2017). The study identified intensified winter monsoon events and sea-level rise impacts on local currents and marine primary productivity. However, the dinoflagellate cyst record could not be adequately compared with other regions and paleoceanographic proxies due to its low resolution. In this study, we analyzed dinoflagellate cysts in an additional 83 samples from the sediment core of Li et al. (2017) to (1) provide a high-resolution dinoflagellate cyst record of paleoceanographic conditions over the past 12,500 years in the northern SCS; (2) quantitatively reconstruct SST, SSS, and PP based on the updated dinoflagellate cyst database of surface sediments; (3) identify the major controlling factors on PP in the northern SCS by comparing our record with reconstructed SST and SSS from other proxies in the region and adjacent areas.

## 2. Regional setting

The SCS is one of the largest marginal seas in the western Pacific, covering an area of  $\sim 3.5 \times 10^6 \text{ km}^2$  from the Tropic of Cancer to the Equator (e.g., Wang and Li, 2009). The Mekong, the Pearl, and the Red (Song Hong) Rivers as well as other smaller rivers transport high volumes of terrestrial material to the well-developed subaquatic deltas in the wide continental shelves of the SCS (e.g., Wang and Li, 2009; Li et al., 2017). Our study area is located at the upper part of northeastern continental slope in a region of relatively high sediment accumulation rates (Fig. 1) (e.g., Wang et al., 2008).

Water temperature in the SCS is controlled by the tropical East Asian Monsoon, with maximum and minimum SSTs occurring in July and January, respectively (e.g., Xie et al., 2003; Fang et al., 2006). Due to the different water masses, the SCS exhibits high SST and low SSS in the south and low SST and high SSS in the north (Fig. 2) (e.g., Xie et al., 2003). In winter monsoon (October–April), an intense western boundary current flows southward toward the continental slope, transporting cold waters from the north and creating a distinct cold-water tongue (Fig. 3) (Liu et al., 2004). Higher SSS can be observed in the northern part of the SCS due to the influence of the Kuroshio Current, and SSS declines southward due to increasing precipitation. The SSS gradient between the north and the south weakens during the summer monsoon (May–September) (e.g., Wang and Li, 2009).

The current surface-water circulation in the SCS is predominantly wind-forced by the northeast winter and southwest summer monsoons (Caruso et al., 2006). During winter, the circulation is characterized by a basin-wide cyclonic gyre and a southwestward coastal current. In summer, the basin-wide circulation splits into a weakened cyclonic gyre in the north and a strong anti-cyclonic gyre in the south, and coastal currents flow northeastward (Fig. 3) (e.g., Qu

et al., 2002). The prevailing monsoon system coupled with the Ekman effect results in winter upwelling off the islands of Borneo, Luzon, and Taiwan, and summer upwelling along the Vietnamese coast and off South China (e.g., Ndaï et al., 2016). The surface water of the SCS exchanges freely with those of neighbouring seas. Deeper water flows into the SCS primarily from the western Philippine Sea through the Luzon (or Bashi) Strait, and an anti-cyclonic current flows along the bottom of the northern slope (Fig. 1). In addition, the Kuroshio Current flows northward along the coast of Luzon Island and branches into the SCS through the Luzon Strait (Yuan et al., 2002) (Fig. 3).

In the SCS, PP is dominantly influenced by nutrient availability in the upper water column. Satellite-based annual PP is more than  $200 \text{ g C m}^{-2}$  on the continental shelf-slope and  $\sim 100\text{-}150 \text{ g C m}^{-2}$  in the basin (<http://marine.copernicus.eu/services-portfolio/access-to-products/>). The PP in winter is much higher than in the summer. During winter, the PP is higher than  $600 \text{ mg C m}^{-2} \text{ day}^{-1}$  in continental shelf-slope and the highest PP, reaching up to  $\sim 1300 \text{ mg C m}^{-2} \text{ day}^{-1}$ , occurs in the northern coastal water of Borneo Island and surrounding Taiwan Island (Fig. 3). In summer, the PP is  $\sim 230\text{-}500 \text{ mg C m}^{-2} \text{ day}^{-1}$ . The winter PP contributes to more than 40% to the annual PP in the northern SCS (Zhang et al., 2016). Observations and numerical evidence showed that the seasonal variation in PP is mainly controlled by the East Asian Monsoon (e.g., Liu et al., 2002). During winter monsoons, the upper photic zone is eutrophic and has a higher marine PP because of the strong northeastern wind. In summer monsoon seasons, hotter and less dense surface water is continually heated and the upper water column becomes strongly stratified and oligotrophic (e.g., Liu et al., 2002; Zhang et al., 2016).

### 3. Materials and methods

### 3.1. Sediment core and laboratory measurements

The gravity core GLW31D (20° 1'57.90"N, 115° 27'52.92"E, at 1187 m water depth) was retrieved from the northern SCS in 2012 and the length of the core was 2.4 m, covering the last 12,500 years (Fig. 1).

The core chronology was established through 11 accelerator mass spectrometry (AMS)  $^{14}\text{C}$  measurements performed by Beta Analytic Inc. The age model calibrations were described in Li et al. (2017) (Fig. 4). The sedimentation rates were calculated based on the age-depth linear model. The accumulation rates varied from  $\sim 7 \text{ cm kyr}^{-1}$  to  $\sim 42 \text{ cm kyr}^{-1}$ , with considerably higher rates of  $\sim 347 \text{ cm kyr}^{-1}$  in the lower part of the core (Fig. 4). The thickness of each analysed for dinoflagellate cyst sample is 2 cm, representing  $\sim 125$  to 290 years on average.

The grain size was measured using a Laser Particle Analyzer Mastersizer 2000 (Marvern, U.K.). The core mainly consisted of dark gray silt and clay (relative contents of  $\sim 70\%$  and  $\sim 26\%$ , respectively) and a low sand content ( $< 5\%$ ) (Fig. 5). The mean grain size varied from  $6.8 \phi$  to  $7.2 \phi$ , and turbidity deposits were completely absent. Clay content increases to the maximum from 12,500 to 9900 cal yr BP as well as  $\phi$  values of the mean grain size. On the contrary, silt content decreased to the minimum in this stage. Sand content kept low values ( $< 1\%$ ). From  $\sim 9900$  to  $\sim 5500$  cal yr BP decreases in the mean grain size and clay content were observed, and silt content increased gradually. After 5500 cal yr BP, the contents of clay, silt and sand were fluctuated at  $\sim 25\%$ ,  $70\%$  and  $3\%$ , respectively (Fig. 5).

To measure the bulk intensities of major geochemical elements, the sediment core was scanned continuously at 1-cm resolution with an X-ray fluorescence (XRF) scanner (AVAATECH, Den Burg, Netherlands) at Tongji University (China). To avoid both contamination of the XRF scanner and sediment desiccation, the surface of the split core was

protected with a 4- $\mu\text{m}$  thick SPEXCerti Prep Ultralene1 foil. The scanner sensor covered an area of 10 x 15 mm every 30 seconds with a generator setting of 10 kV and 30 kV (Richter et al., 2006). Elements were normalized to aluminum (Al), as the number of individual elemental counts could be influenced by sediment inhomogeneity, including water content, organic content, grain-size distribution, and irregularities on the core surface (e.g., Tjallingii et al., 2007; Ziegler et al., 2008). Three notable stages with high-frequency variations in Si/Al, Fe/Al, Ba/Al, Ti/Al and K/Al ratios were observed in the core: at 11200-8700, 6800-5500, and 2700–2200 cal yr BP (Fig. 5).

We analyzed additional 83 samples to the original low-resolution dinoflagellate cyst record of 27 samples from the same core and improved the resolution from millennial to centennial scale (Li et al., 2017). To obtain a continuous record, we applied the same laboratory techniques for extracting and analyzing dinoflagellate cysts. The standardised technique, described in Pospelova et al. (2010), was used on all 110 samples. All samples were treated with room-temperature HCl (10%) and HF (48%) to remove carbonates and silicates, respectively (Price et al., 2016). Finer and coarser particles were removed by sieving through a 120  $\mu\text{m}$  and a 10  $\mu\text{m}$  Nitex nylon mesh, respectively. We added exotic *Lycopodium* spores (18,584 grains/tablet) before chemical treatment to estimate dinoflagellate cyst concentrations and fluxes (e.g., Mertens et al., 2009, 2013). The details of the preparation method are described in Li et al. (2017). The residues were mounted to permanent slides using glycerine jelly for microscopy observations. We counted between 300 and 469 dinoflagellate cysts per sample, with an average of 320 cysts. Dinoflagellate cysts were identified according to the descriptions from a number of peer-reviewed sources (e.g., Matsuoka, 1988; He and Sun, 1991; McMinn, 1991; Zhao and Morzadec-Kerfourn, 1992a, 1992b, 1994, 2009; Mao and Harland, 1993; Kokinos and Anderson, 1995;

Head, 1996; Zonneveld et al., 1997; Head and Westphal, 1999; Rochon et al., 1999; Esper and Zonneveld, 2002; Pospelova and Head, 2002; Matsuoka et al., 2009; Pospelova and Kim, 2010; Verleye et al., 2011; Furio et al., 2012; Zonneveld and Pospelova, 2015; Gurdebeke et al., 2020; Van Nieuwenhove et al., 2020). All smooth round brown cysts were grouped as *Brigantedinium* spp., and folded brown cysts with obscured horns and/or granulated brown surfaces were grouped as cysts of *Protoperidinium* spp. In this study, taxa of *Cryodinium?* *matsuokai* (Uddandam et al., 2020), *Cryodinium?* *meridianum* in Li et al. (2020) and *?Cryodinium meridianum* in Li et al. (2018) were grouped as *Cryodinium?* spp., which differ from *Cryodinium matsuokai* (Esper and Zonneveld, 2002) in having high parasutural septa (Plate 1). Cysts produced by autotrophic (phototrophic) and heterotrophic dinoflagellates were referred to as autotrophic taxa and heterotrophic taxa, respectively. The relative abundances of each dinoflagellate cyst taxon were calculated as percentages of the total counted cysts. Dinoflagellate cyst concentrations (cysts g<sup>-1</sup>) were calculated using the formula:  $C_m = (L_{total} * D_{counted}) / (L_{counted} * G)$ , where  $C_m$  is the cyst concentration.  $L_{total}$  is the total number of *Lycopodium* spores added to the sample.  $L_{counted}$  and  $D_{counted}$  are the numbers of counted *Lycopodium* grains and dinoflagellate cysts in each sample.  $G$  is the dry weight of each sample. The volumes of each sample were also measured to estimate dinoflagellate cyst fluxes ( $F$ ; cysts cm<sup>-2</sup> yr<sup>-1</sup>) that were calculated by using the following formula  $F = (L_{total} * D_{counted}) / (L_{counted} * V * S_{rate})$ , where  $V$  is the volume of each sample and  $S_{rate}$  is the sediment accumulation rate of each sample. More details can be found in Li et al. (2017).

### 3.2. Statistical analyses

Principal component analysis (PCA) was performed on logarithmically transformed relative abundances of dinoflagellate cysts in the sediment core using CANOCO 4.5 (ter Braak and Smilauer, 2002). Prior to the PCA, a detrended correspondence analysis (DCA) was conducted to test the characteristics of the cyst assemblage variability. The application of PCA was justified, as the length of the first gradient was 1.0 standard deviations of DCA, indicating linear variability in the data.

We applied the modern analog technique (MAT) using software C<sub>2</sub> (Juggins, 2007), to quantitatively estimate SST, SSS and PP, based on the dinoflagellate cyst assemblages from the core GLW31D. Before the reconstruction, we used the modern analog technique (MAT) to evaluate the accuracy of the reconstruction of oceanographic parameters of the northern Pacific dataset which was formed by combining 359 sites in the Pacific from de Vernal et al. (2020) and 39 sites from Li et al. (2020) (Fig. 1a).

The taxonomy of Van Nieuwenhoe et al. (2020) was applied as a standard to merge the datasets of Li et al. (2020) and de Vernal et al. (2020). A few dinoflagellate cyst taxa from Li et al. (2020) are not in the de Vernal et al. (2020) dataset, and we added *Dapsilidinium pastielsii* and *Spiniferites hyperacanthus* into the dataset. de Vernal et al. (2020) grouped *Spiniferites hyperacanthus* into *Spiniferites mirabilis*. However, *Spiniferites hyperacanthus* of Li et al. (2020) is different from *Spiniferites mirabilis* by slender processes and a lack of antapical flange (see the images 7 and 13 in Plate 12 of Li et al. (2017), images 6, 8 and 9 in Plate 2 of Li et al. (2020)) and therefore both taxa are remained in the Pacific dataset. Taxa that were identified as different species were grouped into more common taxa. For example, *Lingulodinium hemicystum* in Li et al. (2020) was identified as *Lingulodinium machaerophorum* in Wu and Sun (2005), and *Lingulodinium* sp. A was identified as *Lingulodinium machaerophorum* in Kawamura (2002). So,

all these species were grouped into *Lingulodinium machaerophorum*. Taxa of which identification was hampered by preservation issues, were grouped into their genus level, for example, *Dubridinium cavatum* and *D. caperatum* were grouped into *Dubridinium* spp. Those taxa identified as type-A, -B... were all grouped to genus level. Taxa were updated to cyst-based taxonomy, for example, cyst of *Protoperidinium oblongum* was grouped into *Votadinium* spp.

Environmental parameters used in the combined database are SST, SSS, and PP in February and August (SST-Feb, SST-Aug, SSS-Feb, SST-Aug, PI -Feb, PP-Aug) and annual PP (PP-An) from the World Ocean Atlas 2013 (WOA13; <https://www.nodc.noaa.gov/OC5/woa13/woa13data.html>) (de Vernal et al. (2020) and monthly products of GLORYS, which is a global ocean eddy-resolving model (1/12° horizontal resolution and 50 vertical levels) with reanalysis of data on satellite sea surface temperature, sea surface height and sea ice (<http://marine.copernicus.eu/services-portfolio/access-to-products/>) (Li et al., 2020) (Supplementary Information Table S1). The primary production values are the monthly depth-integrated Chlorophyll-*a* concentration derived from GLODAPv2 (1/4° horizontal resolution and 75 vertical levels), which is a 3-D global biogeochemical model driven by hydrodynamic parameters from GLORYS (Behrenfeld and Falkowski, 1997; <http://marine.copernicus.eu/services-portfolio/access-to-products/>).

CCA was conducted on the combined dinoflagellate cyst abundances and environmental parameters to reassess their relationship. This multivariate statistical analysis was selected based on the initial DCA result which showed the length of the first gradient was 3.82 for standard deviations and indicated the unimodal character of dinoflagellate cyst variability. The relative abundances of dinoflagellate cyst assemblages were logarithmically transformed for each sample (see details on this procedure in de Vernal et al. 2001, 2020). The CCA results showed that SST,

SSS, and PP in February and August as well as annual PP are significantly correlated ( $P < 0.05$ ) with the first two CCA axes (Supplementary Information Fig. S1). It was found that SSTs are the most important environmental factors influencing the distribution of dinoflagellate cysts, which separates the samples of tropical Pacific regions from others in the term of latitudes (Fig. S1). SST-Feb is significantly positively correlated with SST-Aug, and SSS-Feb is significantly correlated with SSS-Aug. SSSs are negatively correlated with PP-Aug and PP-An. SSTs are slightly positively correlated with PP-Feb (Fig. S1). The first CCA axis correlates positively with SSTs and the taxa of *Polysphaeridium zoharyi* (Pzoh), *Lingulodinium machaerophorum* (Lmac), *Spiniferites delicathus* (Sdel), *Stelladinium* spp. (Stel), *Buettatodinium spongium* (Bspo), cysts of *Protoperidinium nudum* (Pnud), *Echinidinium mansparantum* (Etra), *Echinidinium granulatum* (Egra), *Echinidinium aculeatum* (Facu) and negatively with cysts of *Pentapharsodinium dalei* (Pdal), *Islandinium cezare* (Icez), *Spiniferites elongatus* (Selo), cysts of *Polykrikos* sp.-Arctic morphotype (Pacr), *Operculodinium centrocarpum* sensu Wall and Dale (1966) (Open). The second axis correlates positively with PP-An, PP-Aug and the following taxa: *Atlanticodinium striaticonulum* (Ojan), *Spiniferites bulloideus* (Sbul), *Operculodinium israelianum* (Oistr), *Spiniferites bentorii* (Sben), cysts of *Protoperidinium* spp. (Peri), *Dubridinium* spp. (Dubr), cysts of *Protoperidinium fukuyoi* (Cysa), *Trinovantedinium variabile* (Tvar), and *Quinquecuspis concreta* (Qcon). The second axis correlates negatively with SSS-Feb and SSS-Aug as well as the following taxa: *Dapsilidinium pastielsii* (Dpas), *Tuberculodinium vancampoae* (Tvan), *Operculodinium longispinigerum* (Olon), *Spiniferites hyperacanthus* (Shyp), *Spiniferites mirabilis* (Smir), *Impagidinium paradoxum* (Ipar), *Impagidinium* spp. (Ispp), *Impagidinium aculeatum* (Iacu), *Impagidinium patulum* (Ipat), *Nematosphaeropsis labyrinthus* (Nlab), *Spiniferites belerius* (Sbel) and *Spiniferites* sp. granular type (Sgra).

Only those taxa that appeared with >1.5 % in the sediment core were selected to build a model and evaluate its accuracy for the reconstruction. Some others, rare species were further grouped, for example, *Spiniferites pacificus*, *S. delicatus*, and *S. belerius* were grouped into *Spiniferites* spp. (Supplementary Information Tables S1 and S2). All sites of the northern Pacific were included (Supplementary Information Table S3). Bootstrapping run 1000 times for validation and the number of closest analogues is ten for reconstruction (Supplementary Information Table S4). Compared with other methods, the estimates from MAT were more accurate. For example, the coefficients of linear correlation between the estimates and the observations show that the estimates from models of MAT are the best with  $R^2$  ranging from 0.87 to 0.89 for SSSs, from 0.93 to 0.94 for SSTs, and from 0.61 to 0.70 for PPs. When compared, the coefficients of estimates from models of weighted averaging partial least squares (WAPLS) are much lower with  $R^2$  ranging from 0.44 to 0.67 for SSSs, from 0.76 to 0.85 for SSTs, and from 0.27 to 0.56 for PPs (Supplementary Information Table S4). The standard deviations of estimates from MAT are much smaller than those from WAPLS (Supplementary Information Table S4). Therefore, we adapted the models of MAT rather than others after several trials. The relationships between estimates from MAT and observed data are shown in Fig. 8. The models of MAT were then run using the dinoflagellate cyst relative abundance datasets from core GLW31D (Supplementary Information Table S5) to reconstruct the paleoceanographic parameters in the SCS.

## 4. Results and interpretations

### 4.1. Dinoflagellate cyst assemblages

The total concentrations of dinoflagellate cysts varied from 398 to 3165 cysts  $g^{-1}$ , with an average of 1216 cysts  $g^{-1}$ . The total fluxes ranged from 3 to 770 cysts  $cm^{-2} y^{-1}$  and showed a similar trend to that of the sedimentation rates, with higher values at ~10,000–8500 cal yr BP and ~6800–5500 cal yr BP (Figs. 4 and 5). Five dinoflagellate cyst zones (DI to DV) and ten subzones (DIa to DVc) were identified in core GLW31D based on constrained cluster analysis (CONISS) results and the visual inspection of cyst assemblages (Fig. 6).

Zone DI (~12,500–9900 cal yr BP) was characterized by the highest total cyst concentrations (~1860 cysts  $g^{-1}$ ) and the highest relative abundances and concentrations of total *Impagidinium* (~7%, ~120 cysts  $g^{-1}$ ), consisting largely of *I. patulum* and *I. striatum*. Most *Spiniferites* species and *Lingulodinium hemicystum* showed low abundances in this interval (Fig. 6). Heterotrophic taxa showed high abundances and autotrophic taxa had low relative abundances, resulting in the highest ratio of heterotrophic to autotrophic taxa. The highest percentages and concentrations of heterotrophic taxa and the lowest autotrophic taxa were observed in DIb (~11,000 to ~10,400 cal yr BP), different from subzones of DIa and DIc. The total cyst concentration continuously declined from the highest ~2070 cysts  $g^{-1}$  in DIa (~12,500–11,000 cal yr BP) to ~1840 cysts  $g^{-1}$  in DIb, and to ~1300 cysts  $g^{-1}$  in subzone DIc (~10,500–9900 cal yr BP).

Zone DII (~9,900–6800 cal yr BP) showed an increasing trend in autotrophic taxa and a decreasing trend in heterotrophic taxa. The abundances of total *Impagidinium* notably declined (~3%, ~40 cysts  $g^{-1}$ ). Zone DII was divided into two subzones DIIa and DIIb. Subzone DIIa (~9900–8700 cal yr BP) showed higher total cyst fluxes, with an average of 41 cysts  $cm^{-2} y^{-1}$ . Subzone DIIb (~8700–6800 cal yr BP) showed slightly higher relative abundances of autotrophic

taxa and *Spiniferites* spp. and lower abundances of heterotrophic taxa, *Brigantedinium* spp. and *Dubridinium* spp. The concentrations of autotrophic taxa were similar in the two subzones.

Zone DIII (~6800–5500 cal yr BP) was characterized by the highest abundances of *Dapsilidinium pastielsii*, reaching maximum relative and absolute abundances of 21% and 219 cysts g<sup>-1</sup>, respectively. Autotrophic taxa showed the highest abundances, and heterotrophic taxa showed the lowest abundances in this zone. Accordingly, the ratio of heterotrophic to autotrophic taxa was at the lowest level of ~0.5.

Zone DIV (~5500–2700 cal yr BP) was characterized by decreases in the relative abundances and absolute abundances of autotrophic taxa and increases in the relative abundances of heterotrophic taxa. Both relative and absolute abundances of *Dapsilidinium pastielsii* declined noticeably. Subzone DIVb (~3800–2700 cal yr BP) differed from subzone DIVa (~5500–3800 cal yr BP) due to the decrease in the relative abundances and absolute abundances of autotrophic taxa and the increase in the relative abundances of heterotrophic taxa. The relative and absolute abundances of *Dapsilidinium pastielsii*, *Operculodinium centrocarpum* sensu Wall and Dale 1966, *Polysphaeridium zoharyi*, *Spiniferites hyperacanthus*, *Spiniferites mirabilis*, *Spiniferites ramosus*, and *Spiniferites* spp. in subzone DIVb were all lower than those of subzone DIVa. The relative abundances of *Brigantedinium* spp. in subzone DIVb (~29%) were higher than those in subzone DIVa (~23%).

Zone DV (after ~2700 cal yr BP) was characterized by the lowest total fluxes and lower concentrations of autotrophic taxa, averaging 6 cysts cm<sup>-2</sup> y<sup>-1</sup> and 796 cysts g<sup>-1</sup>, respectively. The relative abundances of heterotrophic taxa, *Brigantedinium* spp., *Echinidinium* spp., and cysts of *Protoperidinium* spp. generally increased. We divided this zone into subzones DVa (~2700 – 1500 cal yr BP), DVb (~1500–1000 cal yr BP) and DVc (after ~1000 cal yr BP) based on the

initial increase followed by a notable decrease in the percentages and concentrations of autotrophic taxa, *Lingulodinium hemicystum*, *Polysphaeridium zoharyi*, and *Spiniferites* spp. In contrast, the relative abundances of heterotrophic taxa decreased from ~53% in subzone DVa to ~34% in subzone DVb, followed by an increase to ~58% in subzone DVc. Correspondingly, *Brigantedinium* spp. decreased from ~33% to ~17%, followed by an increase to ~34%. The ratio of heterotrophic to autotrophic taxa declined from an average of 1.19 in subzone DVa to 0.53 in DVb, which then increased to 1.40 in DVc.

#### 4.2. PCA results

The first principal component of the PCA explained 31.6% of the variance in the dinoflagellate cyst data (Figs. 5 and 6). Many autotrophic taxa, such as *Dapsilidinium pastielsii*, *Spiniferites hyperacanthus*, *Spiniferites ramosus*, *Lingulodinium* spp., *Polysphaeridium zoharyi*, *Operculodinium? longispinigerum*, *Operculodinium israelianum*, *Operculodinium centrocarpum* sensu Wall and Dale 1966, and *Impagidinium paradoxum*, showed high positive PCA1 scores. The heterotrophic taxa, such as *Brigantedinium* spp., *Dubridinium* spp., cysts of *Protoperidinium* spp., *Cryodinium?* spp., and *Quinquecuspis concreta*, showed high negative PCA1 scores (Fig. 7). The autotrophic taxa in the positive PCA1 group, particularly with the highest scoring as *Dapsilidinium pastielsii*, are associated with higher SST and SSS, and lower PP in the western Pacific (Supplementary Information Fig. S1) (e.g., Mertens et al., 2014; Li et al., 2017, 2020). In contrast, the heterotrophic taxa in the negative PCA1 group are associated with lower SST and higher PP in upwelling areas (e.g., Li et al., 2020).

The second principal component (PCA2) explains only 9.8% of the variance in the cyst data (Figs. 5 and 6). *Impagidinium patulum*, *Impagidinium* spp., *Impagidinium striatum*, and

*Impagidinium paradoxum* were positively loaded on the PCA2 axis and represent open marine and low nutrient settings (e.g., Zonneveld et al., 2013). In the SCS, these taxa are associated with stratified water influenced by the Kuroshio Current, which carries warm and highly saline low-nutrient water from the western Pacific to the northern SCS (Li et al., 2017, 2020).

In comparison, the autotrophic taxa *Spiniferites mirabilis*, *Spiniferites* spp., and *Polysphaeridium zoharyi*, and heterotrophic *Votadinium* spp., *Echinidinium* spp., *Selenopemphix quanta*, *Selenopemphix nephroides*, *Trinovantedinium applanatum*, and cysts of *Protoperidinium* spp. were negatively loaded on the PCA2 axis. These taxa are associated with high chlorophyll-*a* concentrations and PP in the SCS (Li et al., 2018, 2020). *Spiniferites* spp. and *Spiniferites mirabilis*, which have higher negative scores, are associated with cooler winter waters and have been reported in shelf-break areas influenced by internal waves (Li et al., 2020). The negative PCA2 axis therefore indicates weaker water column stratification due to reduced influences of the Kuroshio Current (e.g., Li et al., 2020).

#### 4.3. Quantitative reconstructions of SST, SSS, and PP

The quantitative estimates of SST, SSS, and PP in February and August showed high-frequency changes prior to ~6800 cal yr BP (Fig. 9). SSTs were the lowest at the beginning of the Holocene and gradually increased after ~6800 cal yr BP, respectively (Fig. 9a and b). SSS-Feb was generally stable with high-amplitude fluctuations during the early Holocene (Fig. 9c). SSS-Aug reached a maximum at ~12,500 cal yr BP and gradually declined to the lowest at ~6800 cal yr BP; this was then followed by a slight increase (Fig. 9d). All PP estimates reached a maximum at ~12,500 cal yr BP (Fig. 9e-g). PP-Feb and PP-An showed similar trends, decreasing to minimum values at ~6800–5000 cal yr BP and then increased to present-day levels (Fig. 9e

and g). PP-Aug declined, but remained stable after ~6800 cal yr BP (Fig. 9f). We identified a notable short-term change at ~2500 cal yr BP characterized by a decrease in SST and an increase in SSS and PP after ~6800 cal yr BP (Fig. 9a-g).

## 5. Discussion

### 5.1. Paleoceanography of the northern SCS before ~6800 cal yr BP

The sediment components were generally very fine with the minimum mean grain size  $\phi > 7$  before ~6800 cal yr BP. The content of silt was relative constant before ~11,000 cal yr BP, declined from 11,000 cal yr BP to ~9900 cal yr BP, and then gradually increased to the present level at ~5500 cal yr BP. However, the magnitude of change was only ~5%. Clay content changed in an opposite (Fig. 5). Based on the dinoflagellate cyst assemblages and the general trends of the estimated oceanographic parameters, this study identified three notable oceanographic stages: 1) high-variability environmental changes prior to ~6800 cal yr BP (zones DI-DII), 2) stable conditions from ~6800 to ~5000 cal yr BP (zone DIII), and 3) some instability after ~5000 cal yr BP (zones DIV-DV) (Figs. 5 and 8). These stages correspond to the timings of relative onshore sea-level change in the region, including 1) a sea-level rise (I), 2) a relatively stable highstand (II), and 3) a slight sea level drop (III) (Fig. 9h) (e.g., Liu et al., 2004; Zong, 2004; Tanabe et al., 2006; Hanebuth et al., 2011). This trend is in agreement with previous pollen, spores, and dinoflagellate cyst records in the SCS (Li et al., 2017). Three intervals may be controlled by the changes in nutrients carried by rivers or coastal and oceanic currents, which were induced by the changes in the sea level and monsoon systems.

High PP was observed between ~12,500 cal yr BP and ~10,400 cal yr BP (subzones DIa and DIb) as reflected by the highest concentrations of total dinoflagellate cysts and *Brigantedinium* spp. (Figs. 5 and 6). High abundances of *Brigantedinium* spp. are typical of elevated nutrient supply (e.g., Harland, 1983; Dale, 1996; Mudie and Harland, 1996). For example, the analysis of seasonal dinoflagellate cyst production off Taiwan showed that both PP and *Brigantedinium* spp. abundance increased under elevated riverine discharge during summer (Li et al., 2018). Moreover, *Brigantedinium* spp. generally are more abundant near winter upwelling zones in the SCS (Li et al., 2020). From 12,500–10,400 cal yr BP, estimated PP-Feb and PP-Aug values were relatively higher than the present, which is consistent with the reconstructed PP based on a species of coccolithophores in this region (Zhang et al., 2016). The higher PP than at present was likely due to the closer proximity of the shore and consequent higher terrestrial nutrient inputs (Zhang et al., 2016; Li et al., 2017). The sea level of the SCS at ~12,500 cal yr BP was ~60 m lower than that of the present day (e.g., Tanabe et al., 2006; Hanebuth et al., 2000, 2011). According to the 60 m isobaths, the shoreline would have been ~100 km closer to the core site (GLW31D). The highest pollen concentrations and herb pollen abundances reported for this site also support this interpretation of the closer proximity of the shoreline and enhanced riverine supply compared to that of the present day (Li et al., 2017). Subsequently, higher terrestrial nutrient influxes from rivers would increase marine primary production.

*Impagidinium* species showed the highest abundances from ~12,500 cal yr BP to ~9900 cal yr BP (Fig. 6), and they are characteristic for low nutrient marine environments (e.g., Zonneveld et al., 2013; Zonneveld and Pospelova, 2015). Interestingly, both *Impagidinium* and *Brigantedinium* taxa occurred in high concentrations and relative abundances during this interval. High *Impagidinium* abundances are known to be associated with the increased influence of the

Kuroshio Current, which initiated by the strong wind stress curl off southwest Taiwan in winter (e.g., Yuan et al., 2002; Wu and Hsin, 2012; Li et al., 2020). In northern Philippine Sea, *Impagidinium* taxa were found to be dominant in the dinoflagellate cyst assemblages (Matsuoka, 1981). In winter, the Kuroshio Current carries high salinity and low-nutrient water from the Philippine Sea through the Luzon Strait; it then flows along the shelf break and reaches the study area in the northern SCS (Fig. 3) (e.g., Shaw, 1996; Ning et al., 2004; Caruso et al., 2006). The high abundances of *Impagidinium* taxa infer the greater influence of the Kuroshio Current at the beginning of the Holocene. The low-salinity water from the ECS did not reach the SCS, as the sea level was too low to breach the “sand ridges”, and the Taiwan Strait remained closed (e.g., Cai, 1997; Hsiung and Saito, 2017; Li et al., 2017). During this period, SSS reached a maximum but showed large amplitude fluctuations (Fig. 9). Li et al. (2017) observed a 5% decrease of *Impagidinium* relative abundance in one sample from ~11,700 to ~11,000 cal yr BP; however, the addition of five analyzed samples from this time interval (this study) suggests that the decrease was short-lived, as *Impagidinium* abundances remained generally high during this time (Fig. 6).

The influence of the Kuroshio Current gradually reduced after ~10,400 cal yr BP, inferred by the decreased abundance of *Impagidinium* species (Fig. 6). The sea level was ~30–25 m lower than the present day (e.g., Zong, 2004; Tanabe et al., 2006; Hanebuth et al., 2011) and would have exceeded the western Changyun sand ridge at a water depth of ~50–30 m (Fig. 9h) by that time. However, the Taiwan Strait would have been still restricted to a narrow channel (Hsiung and Saito, 2017). The upward increase in clay content and reduced mean grain size showed by increase in  $\phi$  value also displayed a possible upward deepening environment before ~9900 cal yr BP. However, values of Ti/Al, an indicator of heavy minerals input by rivers, did not

consistently decrease, but had considerable variability, although the values slightly declined in general ~9000 cal yr BP (Fig. 5). This implied that the nearer upwelling or coastal currents than the present likely also contributed nutrients besides of river inputs. After ~9900 cal yr BP, coastal waters from the ECS may have entered the SCS through the Taiwan Strait; this would have reduced the influence of the Kuroshio Current and consequently lowered the abundances of *Impagidinium* species (Fig. 6). The increase in silt content and accumulation rates with the decrease in clay content until ~5500 cal yr BP (Fig. 5) might be associated with strengthened hydrodynamic forces due to the complex current systems of sea level rise and multiple water sources from the SCS, the ECS and the Philippine Sea. Our record provided the evidence that the influence of the Kuroshio Current was likely weaker in the entire Holocene than during the Younger Dryas/Holocene transition. This seems to be different from Liu et al. (2016) who suggested a strengthened Kuroshio Current during deglaciation. *Spiniferites* species in surface sediments of the SCS showed highest abundances near summer upwelling zones and shelf-break areas where vertical water exchange strongly exchanged and bottom nutrient were transported to the sea surface (Li et al., 2020). Therefore, the increased abundances of autotrophic taxa and *Spiniferites* species from 10,400 to 9900 cal yr BP could be associated with reduced water column stratification because of an increased water exchange between the ECS and the SCS after the Taiwan Strait opened (Figs. 5 and 6). A slightly increase in the concentrations and relative abundances of total *Impagidinium* indicated an enhanced influence from Kuroshio Current during ~8700-6800 (DIIb) (Fig. 6), in which PP continuously declined (Fig. 8). Zhang et al. (2016) interpreted the decreasing PP since the middle Holocene was induced by injecting oligotrophic Kuroshio water masses into the northern SCS because of more frequent El Niño-Southern-Oscillation (ENSO) events. It is different from the decreasing PP in the early Holocene

which was resulted from reduced river inputs and weakening the East Asian winter monsoon (Zhang et al., 2016; Li et al., 2017). In addition, all of the SST, SSS and PP quantitative estimates displayed large amplitude shifts before ~8500 cal yr BP, and their max-min differences were several to ten times of those after ~8500 cal yr BP (Fig. 9). Thus, our dinoflagellate cyst record indicated that the environmental/oceanographic conditions were much more unstable in the early Holocene as the sea-level rose rapidly. This unstable pattern of the Holocene was also observed in the earlier regional studies by Wang et al (1999) and Jiang et al. (2014).

## **5.2. Holocene oceanographic conditions and climate events after ~6800 cal yr BP**

Total dinoflagellate cyst concentrations and the reconstructed SST, SSS, and PP records were relatively stable since ~6800 cal yr BP (Figs. 5 and 8). The lowest PP values during ~6800–5000 cal yr BP may be due to the less nutrient input, increased distance between the core site and the Pearl River (the highest terrigenous source in the study area), as the most landward shoreline of the Pearl River deltaic plain was identified at ~6800 cal. yr BP (Zong et al., 2009).

Paleoceanographic records from other sediment cores in the northern SCS also showed the similar patterns of environmental stability after ~7500–6500 cal yr BP, recorded in the SSS and diatom-based summer SSS data from core 17942 (Wang et al., 1999; Jiang et al., 2014), TEX86– and UK37'-based SSTs from core MD97-2146 (Shintani et al., 2011), alkenones-based SST from core NS02G (Kong et al., 2014), pollen fluxes from core MD05-2906 (Dai and Weng, 2015),  $\delta^{13}\text{C}$  from cores HKUV10 and HKUV 11, and SST from core HKUV11 (Xiong et al., 2018a), as well as from sediment compositional proxies in core PC338 located offshore of Hainan Island (Li et al., 2019). These observations may be associated with the stabilization of regional RSL after ~7000 cal yr BP (Liu et al., 2004a; Zong, 2004; Tanabe et al., 2006; Hanebuth et al., 2011)

or at the present level (Xiong et al., 2018a). In southwestern Taiwan, the maximum transgression occurred at ~6800 cal yr BP (Taira, 1975). In addition, the Taiwan Warm Current was formed after ~7300 cal yr BP, leading to formation of present oceanographic conditions (Hsiung and Saito, 2017). Consequently, this explains why dinoflagellate cyst concentrations and the interpreted oceanographic conditions remained fairly stable compared to that of the preceding interval.

After ~6800 cal yr BP, paleoceanographic conditions showed some regional variability though the changes were not as strong as before. The reconstructed February SST showed a slight and barely noticeable decline, which is in agreement with the weakening Asian monsoon reflected by stalagmite  $\delta^{18}\text{O}$  from Dongge Cave (Fig. 1C) (Wang et al., 2005). However, SSTs generally increased in nearshore and offshore locations away from the Pearl River mouth region (Fig. 10) (Kong et al., 2014; Wu et al., 2017). Winter SST declined and then increased in core 17940 (Jiang et al., 2014), increased in core MD97-2146 (Shintani et al., 2011), and fluctuated in core MD05-9604 (Steinke et al., 2011). These sediment cores are located in different geomorphological settings in the northern SCS (near the Pearl River mouth for HKUB11, offshore near the shelf break for NS02G, and the lower slope or deep sea basin for 17940, MD97-2146, and MD05-2904) and are, therefore, influenced by different currents, water masses, and hydrodynamic forces on sediment depositions (Fig. 1). Compared with the upper slope, the sediments of cores 17940, MD97-2146, and MD05-2904 tend to be more disturbed and greater influenced by the westward flowing bottom currents in the northern SCS (Qu et al., 2006; Zhao et al., 2015) (Fig. 1). Therefore, the discrepancies between the results of each sediment core may be due to localized oceanographic conditions as well as regional climate change. However, we

need to keep in mind that these SST variations are mostly within  $\sim 1^{\circ}\text{C}$  and are beyond reliable detectability limits of used reconstruction methods.

The warmest interval in our study occurred between  $\sim 6800$  cal yr BP and  $\sim 5500$  cal yr BP, indicated by the rapid increase in *Dapsilidinium pastielsii* abundances to maximum values (Figs. 5 and 6). The higher abundances of this thermophilic taxon (Mertens et al. 2014) indicate that this species was more widespread during warm intervals than the present. All the geochemical records showed notable variations during this stage, including Si/Al, Fe/AL, Ba/AL, Ti/Al and K/Al (Fig. 5). Estimated February SSTs were the highest. August PP and SSS were the lowest (Fig. 9). February SSTs are similar in range to the diatom-based winter temperature reconstruction from core 17940 (Fig. 10) (Jiang et al. 2014). Nearshore annual SST fluctuated between  $\sim 26$  and  $27^{\circ}\text{C}$  in core HKUV11 (Wu et al. 2017). However, SSTs in deep basin cores NS02G, MD97-2146, and MD05-9604 showed increasing trends from  $\sim 25.5$  to  $27^{\circ}\text{C}$ , reaching maximum values in the late Holocene (Shintani et al., 2011; Steinke et al., 2011; Kong et al., 2014).

The short-term 4.2-ka event, an abrupt climatic episode from  $\sim 4500$  to  $\sim 3900$  cal yr BP (e.g., Wang et al., 2005; Dean et al., 2015; Railsback et al., 2018; Xiao et al., 2018; Ran and Chen, 2019; Yan and Liu, 2019), was not observed in our cyst record and other locations in the northern SCS except for near shore and offshore locations away from the Pearl River mouth (Fig. 10). However, we identified a potential short-term climatic event at  $\sim 2700$ – $2400$  cal yr BP, with a notable increase in concentrations and relative abundances of *Brigantedinium* spp. in two samples (Fig. 6), an increase in SSS (to 34), and decreases in February and August SSTs by  $\sim 1$ – $1.5^{\circ}\text{C}$  (to  $21.5^{\circ}\text{C}$  and  $28.8^{\circ}\text{C}$ , respectively) (Fig. 10). In addition, an increase in *Pinus* pollen in three assemblages suggested a strengthened winter monsoon of this episode although *Pinus*

pollen record showed slightly earlier (Li et al., 2017). Wang et al. (2005) also identified a weakened Asian monsoon during this interval. A cooling event in response to an intensified Asian winter monsoon was suggested from reduced winter SSTs at core 17940 and reduced annual SSTs in other sediment cores (Fig. 10) (e.g., Shintani et al., 2011; Steinke et al., 2011; Kong et al., 2014). This short-term event was also observed in sediment pollen records from the Gulf of Tonkin, indicating a strengthened winter monsoon and intensified winter currents (Li et al., 2010). In southeastern Hainan, a decrease in riverine input to the shelf was interpreted from a notable decline in Kaolinite content (Xu et al., 2017), and a storm deposit bed was inferred from high Zr/Rb ratios and coarse grain sizes in a coastal lagoon (Zhou et al., 2019). High Sr intensity was also observed in Typhoon-induced deposits from Kamikoshiki, Japan (Woodruff et al., 2009). This climatic event was even identified at high latitudes, such as the observed cold event at ~2500 cal yr BP from core MD952011 in the Norwegian Sea (Calvo et al., 2002). Regardless if this event was a localized or regional, the mechanism that triggered it remains unclear. Wang et al. (2005) attributed the weakened monsoon at ~2500 cal yr BP to changes in solar output, while Woodruff et al. (2009) related it to intensified El Niño activity. Future work is therefore necessary to elucidate the controlling mechanisms of these late Holocene short-term events.

### 5.3. Abrupt high PP events during the late Holocene

High PP and dinoflagellate cyst production generally occurs in high nutrient environments like upwelling regions (e.g., Zonneveld et al., 2010; 2013; Pospelova et al., 2008; Bringue et al., 2013), eutrophication (e.g., Dale 1996, 2001; Matsuoka, 1999, 2001; Pospelova et al., 2002, 2005; Ellegaard et al., 2017), and/or increased light availability (e.g., Dale, 1996; Heikkilä et al., 2016; Li et al., 2018). Highest cyst productivity in the SCS occurs in upwelling areas or along

the northern shelf break where upwelling or internal waves transport nutrients to the sea surface (Li et al., 2020). Elevated summer dinoflagellate cyst production has also been observed off southwest Taiwan because of the high flux of riverine nutrient inputs (Li et al., 2018).

Since the present oceanographic setting was formed, the highest PP was reconstructed in two dinoflagellate cyst assemblages characterized by the increase in relative abundances and concentrations of *Brigantedinium* spp., possibly representing the short cooling event of ~2700–2400 cal yr BP (Figs. 6, 10 and 11). This highest PP is also indicated by the high measured values of Fe/Al, Si/Al, Ba/Al, and Br/Al (Figs. 5 and 11). It was likely associated with more wind-carried terrestrial dust settling on the continental slope and SCS water in response to regional cooling climate (Fig. 11). The high PP during ~2700–2400 cal yr BP might be also associated with intensified human activities in the Late Bronze Age, when the development of tools led to a significant increase in agriculture, hydro-engineering, population, immigration, and warfare. Archaeological and pollen records from Fujian in southeast China indicate significant changes in population densities and deforestation for agricultural development during ~3000–2450 cal. yr BP (Zhao et al., 2017). Agriculture had spread widely to northern Central Asia and high mountain regions during the Bronze Age (~4000–2200 yr BP), as humans were able to adapt to different environments through the use of bronze tools that facilitated the large scale anthropogenic colonization across the high-altitude Tibetan and Yungui Plateaus (e.g., Chen et al., 2014; Spengler III et al., 2016). As well as the northern Inner Asian Mountain Corridor and southern Himalayan/Tibetan routes, agriculture dispersal between China and South Asia also occurred via marine routes along the Chinese coast (via Vietnam to Malaysia) and the southwestward routes across the SCS from the Taiwan Strait (Stevens et al., 2016). Thus,

intensified anthropogenic activities, such as enhanced migration, agriculture, and deforestation, likely influenced riverine nutrient input and PP to our study area ~2700–2400 cal yr BP.

Another slight PP increase was reconstructed at ~1000–600 cal yr BP, and it can be seen in the trends of estimated February and annual PPs, as well as the slightly elevated ratio of heterotrophic to autotrophic taxa (Fig. 11). This short event was also indicated by two dinoflagellate cyst assemblages characterized by the increase in relative abundances and concentrations of *Brigantedinium* spp. However, it was much weaker than the previous PP increase at ~2700–2400 cal yr BP. Nearby records in the SCS and adjacent areas indicate regional climatic warming during ~1000–600 cal yr BP. These records are from the Jinggang area in southeastern China (Huang et al., 2014), Donggou Cave (Wang et al., 2005), the Song Hong (Red River) Delta (Li et al., 2006), Huguangyan Maar Lake (Sheng et al., 2017), the Pearl Estuary (Kong et al., 2014), the Fujian Basin (Yue et al., 2015), Jianfei Cave in Taiwan (Li et al., 2015), the northern SCS (Jiang et al., 2014; Kong et al., 2014; Dai and Weng, 2015), Xiasha and Leizhou Peninsula (Yu et al., 2005; Yan et al., 2015), and the Gulf of Tonkin (Beibuwan) (Li et al., 2010) (Fig. 11). In this study, changes in Fe/Al, Si/Al, and Ba/Al did not coincide with the high PP cyst-based signal during this interval on a warm climatic condition, suggesting that the high PP during ~1000–600 cal yr BP had different controlling mechanisms from that in ~2700–2400 cal yr BP. In addition, intensified deforestation in watershed was reflected by a rapid increase in fern spores and a decrease in arboreal pollen after ~1500 cal yr BP (Li et al., 2017). Therefore, the high PP event in during ~1000–600 cal yr BP should have more enhanced human impacts than that in ~2700–2400 cal yr BP.

Interestingly, the two short-term increased PP events coincided with two dynastic collapses in China at 770–221 BC and AD 907–1368 (grey bands in Fig. 11). The former dynastic collapse

was the Spring and Autumn Period (770–476 BC) and Warring States Period (476–221 BC) that split from the Eastern Zhou Dynasty (770–221 BC). The latter event consisted of more frequent dynastic shifts or split states during the Five Dynasties Period (AD 907–960) and the Liao (AD 916–1125), Northern Song (AD 960–1125), Jin (AD 1115–1234), Southern Song (AD 1127–1279), and Yuan (AD 1279–1368) dynasties (Fig. 11). Large population migration and intensified warfare occurred frequently during the Spring and Autumn Period and the Warring States Period, resulting in the formation of a number of Chinese states. During these turmoil times, large feudal states on the fringes of the empire fought for supremacy, and much of the population also migrated upland. For example, a military force into the southwest of China formed the ancient Dian Kingdom, which existed for ~500 years, in the present Kuming region, on the Yungui Plateau during the late Spring and Autumn Period (Yao, 2008; Yao and Jiang, 2012). There is a parallel between regional environmental changes and the effects they produce on local societies, and vice versa. The Pearl River originates in the Yungui Plateau, and the upper reaches of the Xi branch are located near to the ancient Dian Kingdom. Soil loss due to societal and agricultural activities were likely increased in the Pearl River discharge, resulting in the influx of nutrients to the northern SCS, and a subsequent increase in sea surface PP. However, it is also possible that the sudden climatic event was the main reason for societal collapses (e.g., Zhang et al., 2008; Li et al., 2009; Wang et al., 2010). Extreme abrupt climatic events in the late Holocene were likely affecting socio-economic conditions through the changes to agriculture availability in the East Asian (e.g., Constantine et al., 2019; Qiu et al., 2020), when high-frequency dry / wet shifts or severe droughts / floods were prominent, leading to wars and eventual dynasty collapses (Zhang et al., 2008; Jia et al., 2018). Therefore, a detail research on effects of population migration and agricultural land use on river discharges, as well as

consequent changes in supply of terrestrial nutrient to the northern SCS would help to understand the interaction between short term climatic events, societal collapses and marine primary productivity.

#### **5.4 Limitation of the quantitative estimates**

Microfossil-based quantitative reconstructions of environmental parameters in the past all have uncertainties to some extent and are therefore called “proxies” (e.g., de Vernal et al., 2005; Lin et al., 2006; Verleye et al., 2009; Jiang et al., 2014; Wu et al., 2017; Herbert and Harrison, 2016; Contreras-Rosales et al., 2019). Similarly in our study, for example, we assume that the biological production and adaption to a specific environment remains stable from the past to the present. The sites in the reference datasets range from coasts to open basins and from high latitude to low latitude regions. The sedimentary accumulation rates vary from site to site greatly and this is always taken into account (e.g., de Vernal 2001, 2005, 2013, 2020; Guiot and de Vernal, 2011a, b; Steinke et al., 2011; Telford and Birks, 2011). All samples in the database were collected from the top 1-2-cm sediments, which represents deposition over several years up to even one thousand years (de Vernal et al., 2020; Li et al., 2020). Therefore, the environmental parameters averaged over several decades could not match the time interval at which dinoflagellate cysts were accumulated in some sediment samples. Some cyst assemblages could also contain allochthonous cysts transported by currents and deposited away from the place of origin (e.g., de Vernal 2005). The cyst assemblages from the surface sediments could not represent the real cyst production and dinoflagellate eco-structure. All these limitations unavoidably result in errors of estimates from models, and they are consistent with most of other biological proxies.

Therefore, in this study, we reconstruct paleoenvironmental conditions based on qualitative or semi-quantitative methods through dinoflagellate cyst assemblages and PCA results. For the quantitative estimates from MAT, we cautiously refer to the trends in oceanographic parameters instead of the estimated data, especially before ~6800 cal yr BP when the sedimentary environment and currents were quite different from the present. In addition, only nine sites in the modern datasets where temperatures could be analogue to the transition period and early Holocene in the study area could lead to less accurate estimates of SST when using MAT in this interval. This might explain large amplitude shifts of the SSTs before ~8500 cal yr BP. However, SSSs and PPs, which reconstructed with modern datasets covering their ranges throughout the Holocene, also displayed large-amplitude shifts. Thus, the large amplitude shifts could be associated with other factors, such as the changes in environmental conditions due to the rapid sea-level rise, not only modern dataset limitations for analogue.

## 6. Conclusion

This study is the first to present high-resolution dinoflagellate cyst record covering for the entire Holocene in the SCS. Paleoceanographic conditions were qualitatively and quantitatively reconstructed using the MAT method on both the cyst record of a sediment core and the modern Pacific dinoflagellate cyst database. We identified five dinoflagellate cyst zones and ten subzones based on notable changes in the dinoflagellate cyst assemblages over the last 12,500 years.

The detailed dinoflagellate cyst record indicates that Holocene SST, SSS, and PP changes were predominantly controlled by the sea level fluctuations. We identified an increase in SST and decreases in SSS and PP before ~6800 cal yr BP, reaching SST maximum, and SSS and PP

minima during ~6800–5000 cal yr BP. This was then followed by a slight decline in SST and slight increases in SSS and PP. These intervals coincided with three stages of the sea-level change, including sea-level rise, sea-level stabilization and a slight fall in sea level on the regional scale, respectively. Reconstructed SST, SSS and PP showed high-amplitude variability before ~8500 cal yr BP in response to rapid regional sea level rise; this intensified variability subsequently stabilized under the decelerated sea-level rise.

Prior to ~6800 cal yr BP (zones DI and DII), the dinoflagellate cyst assemblages were predominantly influenced by changes in water masses, sea level and ocean currents. The Kuroshio Current strongly influenced our study site before the opening of the Taiwan Strait at ~9900 cal yr BP, as reflected by the highest *Impagidinium* spp. abundances and high SSS values. The highest PP during the early Holocene was likely due to the high influx of terrestrial nutrients delivered by rivers.

After ~6800 cal yr BP (zones DIII, DIV, and DV), the modern oceanographic setting was formed following the formation of the Taiwan Warm Current and the stabilization of RSL. The warmest interval in the record occurred from ~6800 cal yr BP to ~5500 cal yr BP as reflected by the highest *Dapsilidinium pacificum* abundances.

Our dinoflagellate cyst record does not show the 4.2-ka event, but this is consistent with most regional and local data from the northern SCS. However, a short-term cooling event was identified during ~2700–2400 cal yr BP, and it was characterised by slightly lower SST and higher SSS and PP.

Studied at centennial resolution, the upper section of the core GLW31D allowed us to identify two short elevated PP events occurring at ~2700–2400 cal yr BP and ~1000–600 cal yr BP. These two events were also expressed by increases in the concentrations and relative

abundances of *Brigantedinium* spp. However, the causes of these events were likely different. Both events coincided with two major periods of Chinese dynastic collapses, and anthropogenic activities may have indirectly intensified nutrient fluxes to core site in the SCS. The cooling during ~2700–2400 cal yr BP may have also contributed to the increased PP during this interval.

### **Acknowledgements**

This work was partially funded by the Natural Sciences and Engineering Research Council of Canada (NSERC) through a Discovery grant (RGPIN/6388–2015) to V. Pospelova. L. Liu was partially supported by the National Program on Global Change and Air-Sea Interaction, NMR (No. GASI-GEOGE-05) and National Key R & D Program of China (2016YFB0501703) in this work. NSERC CGS D3 Fellowship (CGSD3-475098–2015) and NSERC Postdoctoral Fellowship (PDF–516186–2018) provided funding for this research to Z. Li.

### **Declaration of interests**

The authors declare that they have no known competing financial interests or personal relationships that could have appeared to influence the work reported in this paper.

### **References**

- Behrenfeld, M.J., Falkowski, P.G., 1997. Photosynthetic rates derived from satellite-based chlorophyll concentration. *Limnology and Oceanography* 42, 1–20.
- Bringué, M., Pospelova, V., Pak, D., 2013. Seasonal production of organic-walled dinoflagellate cysts in an upwelling system: a sediment trap study from the Santa Barbara Basin, California. *Marine Micropaleontology* 100, 34–51.
- Bringue, M., Pospelova, V., Field, D.B., 2014. High resolution sedimentary record of dinoflagellate cysts reflects decadal variability and 20th century warming in the Santa Barbara Basin. *Quaternary Science Reviews* 105, 86–101.

- Cai, B., 1997. “Dongshan Land Bridge” and the earliest human in Taiwan. *Journal of Zhangzhou Teachers College* 3, 31–36 (in Chinese).
- Caron, M., Rochon, A., Montero-Serrano, J.C., St-Onge, G., 2019. Evolution of sea-surface conditions on the northwestern Greenland margin during the Holocene. *Journal of Quaternary Science* 34, 569–580.
- Caruso, M.J., Gawarkiewicz, G.G., Beardsley, R.C., 2006. Interannual variability of the Kuroshio intrusion in the South China Sea. *Journal of Oceanography* 62, 559–575.
- Chen, F.H., Dong, G., Zhang, D. et al. 2014. Agriculture facilitated permanent human occupation of the Tibetan Plateau after 3600 BP. *Science* 347, 248–250.
- Constantine, M., Kim, M., Park, J., 2019. Mid- to late Holocene cooling events in the Korean peninsula and their possible impact on ancient societies. *Quaternary Research* 92, 98–108.
- Contreras-Rosales, L.A., Jennerjahn, T., Steirke, S., Mohtadi, M., Schefuss, E., 2019. Holocene changes in biome size and tropical cyclone activity around the Northern South China Sea. *Quaternary Science Reviews* 215, 45–63.
- Dai, L., Weng, C., 2015. Marine palynological record for tropical climate variations since the late last glacial maximum in the northern South China Sea. *Deep Sea Research Part II: Topical Studies in Oceanography* 122, 153–162.
- Dale, B., 1996. Dinoflagellate cyst ecology: modeling and geological applications. In: Jansonius, J., McGregor, D.C. (Eds.), *Palynology: Principles and Applications*. AASP Foundation, pp. 1249–1275.
- Dale, B., 2001. Marine dinoflagellate cysts as indicators of eutrophication and industrial pollution: a discussion. *Science of the Total Environment* 264, 235–240.

- Datema, M., Sangiorgi, F., de Vernal, A., Reichert, G.J., Lourens, L.J., Sluijs, A., 2019. Millennial-scale climate variability and dinoflagellate-cyst-based seasonality changes over the last similar to 150 kyrs at "Shackleton Site" U1385. *Paleoceanography and Paleoclimatology* 34, 1139–1156.
- de Vernal, A., Turon, J.-L., Guiot, J., 1994. Dinoflagellate cyst distribution in high-latitude marine environments and quantitative reconstruction of sea-surface salinity, temperature, and seasonality. *Canadian Journal of Earth Sciences* 31, 48–62.
- de Vernal, A., Rochon, A., Turon, J.-L., Matthiessen, J., 1997. Organic-walled dinoflagellate cysts: Palynological tracers of sea-surface conditions in middle to high latitude marine environments. *Geobios* 30, 905–920.
- de Vernal, Henry, M., Matthiessen, J., Mudie, P.J., Rochon, A., Boessenkool, K.P., Eynaud, F., Grosfjeld, K., Guiot, J., Hamel, D., Harland, R., Head, M.J., Kunz-Pirrung, M., Levac, E., Loucheur, V., Peyron, O., Pospelova, V., Radi, T., Turon, J.-L., Voronina, E., 2001. Dinoflagellate cyst assemblages as tracers of sea-surface conditions in the northern North Atlantic, Arctic and sub-Arctic seas: The new "n = 677" database and application for quantitative paleoceanographical reconstruction. *Journal of Quaternary Science* 16, 681–699.
- de Vernal, A., Eynaud, F., Henry, M., Hillaire-Marcel, C., Londeix, L., Mangin, S., Matthiessen, J., Marret, F., Radi, T., Rochon, A., Solignac, S., Turon, J.-L., 2005. Reconstruction of sea-surface conditions at middle to high latitudes of the Northern Hemisphere during the Last Glacial Maximum (LGM) based on dinoflagellate cyst assemblages. *Quaternary Science Reviews* 24, 897–924.
- de Vernal, A., Hillaire-Marcel, C., Rochon, A., Fréchette, B., Henry, M., Solignac, S., Bonnet, S., 2013. Dinocyst-based reconstructions of sea-ice cover

concentration during the Holocene in the Arctic Ocean, the northern North Atlantic Ocean and its adjacent seas. *Quaternary Science Review* 79, 111–121.

de Vernal, A., Radi, T., Zaragosi, S., Van Nieuwenhove, N., Rochon, A., Allan, E., De Schepper, S., Eynaud, F., Head, M.J., Limoges, A., Londeix, L., Marret, F., Matthiessen, J., Penaud, A., Pospelova, V., Price, A., Richerol, T., 2020. Distribution of common modern dinoflagellate cyst taxa in surface sediments of the Northern Hemisphere in relation to environmental parameters: The new n=1968 database. *Marine Micropaleontology* 159, 10179, doi:10.1016/j.marmicro.2019.101796.

Dodge, J.D., Harland, R., 1991. The distribution of planktonic dinoflagellates and their cysts in the eastern and northeastern Atlantic-Ocean. *New Phytologist* 118, 593–603.

Ellegaard, M., Dale, B., Mertens, K.N., Pospelova, V., Ribeiro, S., 2017. Chapter 12: Dinoflagellate cysts as proxies for Holocene and recent environmental change in estuaries: Diversity, abundance and morphology. In Weckström, K., Saunders, K.M., Gell, P.A., Gregory Skilbeck, C. (eds.). *Applications of Paleoenvironmental Techniques in Estuarine Studies, Developments in Paleoenvironmental Research* 20, doi:10.1007/978-94-024-0990-1\_12, Berlin, Germany, Springer, p. 295–312.

Esper, O., Zonneveld, K., 2002. Distribution of organic-walled dinoflagellate cysts in surface sediments of the Southern Ocean (eastern Atlantic sector) between the subtropical front and the Weddell Gyre. *Marine Micropaleontology* 46, 177–208.

Fang, G.H., Fang, W.D., Fang, Y., Wang, K., 1998. A survey of studies on the South China Sea upper ocean circulation. *Acta Oceanographica Taiwanica* 37, 1–16.

Fang, G.H., Chen, H.Y., Wei, Z.X., Wang, Y.G., Wang, X.Y., Li, C.Y., 2006. Trends and interannual variability of the South China Sea surface winds, surface height, and surface

- temperature in the recent decade. *Journal of Geophysical Research-Oceans* 111, C11S16, doi.org/10.1029/2005jc003276.
- Furio, E.E., Azanza, R.V., Fukuyo, Y., Matsuoka, K., 2012. Review of geographical distribution of dinoflagellate cysts in Southeast Asian coasts. *Coastal Marine Science* 35, 20–33.
- Geitzenauer, K.R., Roche, M.B., McIntyre, A., 1976. Modern Pacific coccolith assemblages: derivation and application to late Pleistocene paleotemperature analysis. In: R.M. Cline and J.D. Hays (Editors), *Investigations of Late Quaternary Paleoceanography and Paleoclimatology*. Geological Society of America Memoir 145, 423–448.
- Guiot, J., de Vernal, A., 2011. Is spatial autocorrelation introducing biases in the apparent accuracy of paleoclimatic reconstructions? *Quaternary Science Reviews* 30, 1965–1972.
- Guiot, J., de Vernal, A., 2011b. QSR correspondence “Is spatial autocorrelation introducing biases in the apparent accuracy of paleoclimatic reconstructions?” reply to Telford and Birks. *Quaternary Science Reviews* 30, 3214–3216.
- Gurdebeke, P.R., Pospelova, V., Mertens, K.N., Dallimore, A., Chana, J., Louwye, S., 2018. Diversity and distribution of dinoflagellate cysts in surface sediments from fjords of western Vancouver Island (British Columbia, Canada). *Marine Micropaleontology* 143, 12–29.
- Gurdebeke, P.R., Mertens, K.N., Pospelova, V., Matsuoka, K., Li, Z., Gribble, K.E., Gu, H., Bogus, K., Vrielinck, H., Louwye, S., 2020. Taxonomic revision, phylogeny, and cyst wall composition of the dinoflagellate cyst genus *Votadinium* Reid (Dinophyceae, Peridinales, Protoperidiniaceae). *Palynology* 44, 310–335.
- Hanebuth, T., Statterger, K., Grootes, P.M., 2000. Rapid flooding of the Sunda Shelf: A late-glacial sea-level record. *Science* 288, 1033–1035.

- Hanebuth, T.J.J., Voris, H.K., Yokoyama, Y., Saito, Y., Okuno, J., 2011. Formation and fate of sedimentary depocentres on Southeast Asia's Sunda Shelf over the past sea-level cycle and biogeographic implications. *Earth-Science Reviews* 104, 92–110.
- Harland, R., 1973. Quaternary (Flandrian?) Dinoflagellate Cysts from Grand-Banks, Off Newfoundland, Canada. *Review of Palaeobotany and Palynology* 16, 229–242.
- Harland, R., 1983. Distribution Maps of Recent Dinoflagellate Cysts in Bottom Sediments from the North-Atlantic Ocean and Adjacent Seas. *Palaeontology* 26, 321–387.
- Harland, R., Howe, J.A., 1995. Dinoflagellate Cysts and Holocene Oceanography of the Northeastern Atlantic-Ocean. *Holocene* 5, 220–228.
- Harland, R., Asteman, I.P., Morley, A., Morris, A., Harris, A., Howe, J.A., 2016. Latest Quaternary palaeoceanographic change in the eastern North Atlantic based upon a dinoflagellate cyst event ecostratigraphy. *Heliyon* 2, E0014.
- He, C., Sun, X., 1991. Dinoflagellate cysts from quaternary sediments of Nansha, South China Sea. In: The Multidisciplinary Oceanographic Expedition Team of Academia Sinica to the Nansha Islands (Eds.), *Quaternary Biological Groups of the Nansha Islands and the Neighbouring Waters* Science Press, Beijing, China, pp. 266–302, 520–525.
- He, J., Zhao, M., Li, L., Wang, P., Ge, H., 2008. Sea surface temperature and terrestrial biomarker records of the last 260 ka of core MD05-2904 from the northern South China Sea. *China Science Bulletin* 53, 2376–2384.
- Head, M.J., 1996. Chapter 30. Modern dinoflagellate cysts and their biological affinities. In: Jansonius, J., McGregor, D.C. (Eds.), *Palynology: Principles and Applications*. American Association of Stratigraphic Palynologists, Dallas, USA, pp. 1197–1248.

- Head, M.J., Westphal, H., 1999. Palynology and paleoenvironments of a Pliocene carbonate platform: the Clino core, Bahamas. *Journal of Paleontology* 73, 1–25.
- Herbert, A.V., Harrison, S.P., 2016. Evaluation of a modern-analogue methodology for reconstructing Australian palaeoclimate from pollen. *Review of Palaeobotany and Palynology* 226, 65–77.
- Heikkilä, M., Pospelova, V., Hochheim, K.P., Kuzyk, Z.Z.A., Stern, G.A., Barber, D.G., Macdonald, R.W., 2014. Surface sediment dinoflagellate cysts from the Hudson Bay system and their relation to freshwater and nutrient cycling. *Marine Micropaleontology* 106, 79–109.
- Heikkilä, M., Pospelova, V., Forest, A., Stern, G.A., Fortier, L., Macdonald, R.W., 2016. Dinoflagellate cyst production over an annual cycle in seasonally ice-covered Hudson Bay. *Marine Micropaleontology* 125, 1–24.
- Hsiung, K.H., Saito, Y., 2017. Sediment trapping in deltas of small mountainous rivers of southwestern Taiwan and its influence on East China Sea sedimentation. *Quaternary International* 455, 30–44.
- Huang, C.Y., Wu, S.F., Zhao, M.X., Chen, M.T., Wang, C.H., Tu, X., Yuan, P.B., 1997. Surface ocean and monsoon climate variability in the South China Sea since the last glaciation. *Marine Micropaleontology* 32, 71–94.
- Huang, Y., Jiang, H., Sarnthein, M., Knudsen, K.L., Li, D., 2009. Diatom response to changes in palaeoenvironments of the northern South China Sea during the last 15 000 years. *Marine Micropaleontology* 72, 99–109.
- Huang, K., Zheng, Z., Liao, W., Cao, L., Zheng, Y., Zhang, H., Zhu, G., Zhang, Z., Cheddadi, R., 2014. Reconstructing late Holocene vegetation and fire histories in monsoonal region of southeastern China. *Palaeogeography, Palaeoclimatology, Palaeoecology* 393, 102–110.

- Imbrie, J., Kipp, N.G., 1971. A new micropaleontological method for quantitative paleoclimatology: Application to a late Pleistocene Caribbean core. In: K.K. Turekian (Editor), Late Cenozoic Glacial Ages. Yale Univ. Press, New Haven, CT, pp. 71–182.
- Jia, D., Li, Y.K., Fang, X.Q., 2018. Complexity of factors influencing the spatiotemporal distribution of archaeological settlements in northeast China over the past millennium. *Quaternary Research* 89, 413–424.
- Jiang, H., Knudsen, M.F., Seidenkrantz, M.-S., Zhao, M.X., Sha, L.R., Ran, L.H., 2014. Diatom-based reconstruction of summer sea-surface salinity in the South China Sea over the last 15 000 years. *Boreas* 43, 208–219.
- Juggins, S., 2007. C2 Version 1.5: User Guide. Software for ecological and palaeoecological data analysis and visualisation. Newcastle University, Newcastle upon Tyne. pp. 73.
- Kokinos, J.P., Anderson, D.M., 1995. Morphological development of resting cysts in cultures of the marine dinoflagellate *Lingulodinium polyedrum* (= *L. machaerophorum*). *Palynology* 19, 143–166.
- Kong, D., Zong, Y., Jia, G., Wei, G., Chen, M., Liu, Z., 2014. The development of late Holocene coastal cooling in the northern South China Sea. *Quaternary International* 349, 300–307.
- Ledu, D., Rochon, A., de Vernal, A., St-Onge, G., 2008. Palynological evidence of Holocene climate change in the eastern Arctic: a possible shift in the Arctic oscillation at the millennial time scale. *Canadian Journal of Earth Sciences* 45, 1363–1375.
- Ledu, D., Rochon, A., de Vernal, A., St-Onge, G., 2010. Holocene paleoceanography of the northwest passage, Canadian Arctic Archipelago. *Quaternary Science Reviews* 29, 3468–3488.

- Li, H.-C., Zhao, M., Tsai, C.-H., Mii, H.-S., Chang, Q., Wei, K.-Y., 2015. The first high-resolution stalagmite record from Taiwan: Climate and environmental changes during the past 1300 years. *Journal of Asian Earth Sciences* 114, 574–587.
- Li, M., Ouyang, T., Tian, C., Zhu, Z., Peng, S., Tang, Z., Qiu, Y., Zhong, H., Peng, X., 2019. Sedimentary responses to the East Asian monsoon and sea level variations recorded in the northern South China Sea over the past 36 kyr. *Journal of Asian Earth Sciences* 171, 213–224.
- Li, Z., Saito, Y., Matsumoto, E., Wang, Y., Tanabe, S., Zang, L., Vu, Q., 2006. Climate change and human impact on the Song Hong (Red River) delta, Vietnam, during the Holocene. *Quaternary International* 144, 4–28.
- Li, Z., Saito, Y., Dang, P., Matsumoto, E., Vu, Q., 2009. Warfare rather than agriculture as a critical influence on fires in the late Holocene, inferred from northern Vietnam. *Proceedings of the National Academy of Sciences of the United States of America (PNAS)* 106, 11472–11477.
- Li, Z., Zhang, Y., Li, Y., Zhao, J., 2010. Palynological records of Holocene monsoon change from the Gulf of Tonkin (Beibuwan), northwestern of South China Sea. *Quaternary Research* 74, 8–14.
- Li, Z., Pospelova, V., Liu, L.J., Zhou, R., Song, B., 2017. High-resolution palynological record of Holocene climatic and oceanographic changes in the northern South China Sea. *Palaeogeography, Palaeoclimatology, Palaeoecology* 483, 94–124.
- Li, Z., Pospelova, V., Lin, H.-L., Liu, L., Song, B., Gong, W., 2018. Seasonal dinoflagellate cyst production and terrestrial palynomorph deposition in the East Asian Monsoon influenced

- South China Sea: A sediment trap study from the Southwest Taiwan waters. *Review of Palaeobotany and Palynology* 257, 117–139.
- Li, Z., Pospelova, V., Kawamura, H., Luo, C., Mertens, K.N., Hernández-Almeida, I., Yin, K., Wu, Y., Wu, H., Xiang, R., 2020. Dinoflagellate cyst distribution in surface sediments from the South China Sea in relation to hydrographic conditions and primary productivity. *Marine Micropaleontology*, 101815, doi:10.1016/j.marmicro.2019.101815.
- Limoges, A., Kieft, J.F., Radi, T., Ruiz-Fernandez, A.C., de Vernal, A., 2010. Dinoflagellate cyst distribution in surface sediments along the south-western Mexican coast (14.76°N to 24.75° N). *Marine Micropaleontology* 76, 104–123.
- Limoges, A., de Vernal, A., Van Nieuwenhove, N., 2014. Long-term hydrological changes in the northeastern Gulf of Mexico (ODP-625B) during the Holocene and late Pleistocene inferred from organic-walled dinoflagellate cysts. *Palaeogeography, Palaeoclimatology, Palaeoecology* 414, 178–191.
- Lin, D.C., Liu, C.H., Fang, T.H., Tsai, C.H., Murayama, M., Chen, M.T., 2006. Millennial-scale changes in terrestrial sediment input and Holocene surface hydrography in the northern South China Sea ( IMAGES MD972146). *Palaeogeography, Palaeoclimatology, Palaeoecology* 236, 56–73.
- Liu, J., Xiang, R., Chen, M., Chen, Z., Yan, W., Liu, F., 2011. Influence of the Kuroshio current intrusion on depositional environment in the Northern South China Sea: Evidence from surface sediment records. *Marine Geology* 285, 59–68.
- Liu, J., Xiang, R., Chen, Z., Chen, M., Yan, W., Zhang, L., Chen, H., 2013a. Sources, transport and deposition of surface sediments from the South China Sea. *Deep Sea Research Part I: Oceanographic Research Papers* 71, 92–102.

- Liu, J., Li, T., Xiang, R., Chen, M., Yan, W., Chen, Z., Liu, F., 2013b. Influence of the Kuroshio Current intrusion on Holocene environmental transformation in the South China Sea. *Holocene* 23, 850–859.
- Liu, J.P., Milliman, J.D., Gao, S., Cheng, P., 2004a. Holocene development of the Yellow River subaqueous delta, North Yellow Sea. *Marine Geology* 209, 45–67.
- Liu, Q., Jiang, X., Xie, S., Liu, W., 2004b. A gap in the Indo-Pacific warm pool over the South China Sea in boreal winter: Seasonal development and interannual variability. *Journal of Geophysical Research-Oceans* 109, C07012, doi:10.1029/2002JC002179.
- Liu, Z., Tuo, S., Colin, C., Liu, J.T., Huang, C.-Y., Selvaraj, K., Chen, C.-T.A., Zhao, Y., Siringan, F.P., Boulay, S., Chen, Z., 2008. Detrital fine-grained sediment contribution from Taiwan to the northern South China Sea and its relation to regional ocean circulation. *Marine Geology* 255, 149–155.
- Liu, Z., Zhao, Y., Colin, C., Stattegger, K., Wiesner, M.G., Huh, C.A., Zhang, Y., Li, X., Sompongchaiyakul, P., You, C., Huang, C., Liu, J., Siringan, F.P., Le, K., Sathiamurthy, E., Hantoro, W.S., Liu, J., Tuo, S., Zhao, S., Zhou, S., He, Z., Wang, Y., Bunsomboonsakul, S., Li, Y., 2016. Source-to-sink transport processes of fluvial sediments in the South China Sea. *Earth-Science Reviews* 153, 238–273.
- Londeix, L., Herreyre, Y., Turon, J.L., Fletcher, W., 2009. Last Glacial to Holocene hydrology of the Marmara Sea inferred from a dinoflagellate cyst record. *Review of Palaeobotany and Palynology* 158, 52–71.
- Ludmann, T., Wong, H.K., Berglar, K., 2005. Upward flow of North Pacific Deep Water in the northern South China Sea as deduced from the occurrence of drift sediments. *Geophysical Research Letters* 32, L05614, doi:10.1029/2004GL021967.

- Mao, S., Harland, R., 1993. Quaternary organic-walled dinoflagellate cysts from the South China Sea and their paleoclimatic significance. *Palynology* 17, 47–65.
- Marret, F., Zonneveld, K.A.F., 2003. Atlas of modern organic-walled dinoflagellate cyst distribution. *Review of Palaeobotany and Palynology* 125, 1–200.
- Marret, F., de Vernal, A., McDonald, D., Pedersen, T., 2001. Middle Pleistocene to Holocene palynostratigraphy of ODP Site 887 in the Gulf of Alaska, northeast North Pacific. *Canadian Journal of Earth Science* 38, 373–386.
- Marret, F., Rradley, L.R., Tarasov, P.E., Ivanova, E.V., Zenina, M.A., Murdmaa, I.O., 2019. The Holocene history of the NE Black Sea and surrounding areas: An integrated record of marine and terrestrial palaeoenvironmental change. *The Holocene* 29, 648–661.
- Matsuoka, K., 1988. Cyst-theca relationships in the diplopsalid group (Peridinales, Dinophyceae). *Review of Palaeobotany and Palynology* 56, 95–122.
- Matsuoka, K., 1999. Eutrophication process recorded in dinoflagellate cyst assemblages—a case of Yokohama Port, Tokyo Bay, Japan. *Science of the Total Environment* 231, 17–35.
- Matsuoka, K., 2001. Further evidence for a marine dinoflagellate cyst as an indicator of eutrophication in Yokohama Port, Tokyo Bay, Japan. Comments on a discussion by B. Dale. *Science of the Total Environment* 264, 221–233.
- Matsuoka, K., Kawami, H., Nagai, S., Iwataki, M., Takayama, H., 2009. Re-examination of cyst–motile relationships of *Polykrikos kofoidii* Chatton and *Polykrikos schwartzii* Butschli (Gymnodiniales, Dinophyceae). *Review of Palaeobotany and Palynology* 154, 79–90.
- Maynard, M.G., 1976. Relationship between diatoms in surface sediments and the biological and physical oceanography of overlying waters. *Paleobiology* 2, 99–121.

- McMinn, A., 1991. Recent Dinoflagellate Cysts from Estuaries on the Central Coast of New South Wales, Australia. *Micropaleontology* 37, 269–287.
- Meon, H., Pannetier, W., 1994. Palynological Study of the Late Quaternary of Loyalty Basin (Sw Pacific). *Palaeogeography, Palaeoclimatology, Palaeoecology* 111, 135–147.
- Mertens, K.N., Gonzalez, C., Delusina, I., Louwye, S., 2009. 30 000 years of productivity and salinity variations in the late Quaternary Cariaco Basin revealed by dinoflagellate cysts. *Boreas* 38, 647–662.
- Mertens, K.N., Bradley, L.R., Takano, Y., Mudie, P.J., Marret, F., Aksu, A.E., Hiscott, R.N., Verleye, T.J., Mousing, E.A., Smyrnova, L.L., Bagheri, S., Mansor, M., Pospelova, V., Matsuoka, K., 2012. Quantitative estimation of Holocene surface salinity variation in the Black Sea using dinoflagellate cyst process length. *Quaternary Science Reviews* 39, 45–59.
- Mertens, K.N., Takano, Y., Head, M.J., Matsuoka, K., 2014. Living fossils in the Indo-Pacific warm pool: a refuge for thermophilic dinoflagellates during glaciations. *Geology* 42, 531–534.
- Mudie, P.J., Harland, R., 1996. Chapter 21. Aquatic Quaternary. In: Jansonius, J., McGregor, D.C. (Eds.), *Palynology: Principles and Applications*. AASP Foundation, pp. 843–877.
- Mudie, P.J., Rochon, A., 2001. Distribution of dinoflagellate cysts in the Canadian Arctic marine region. *Journal of Quaternary Science* 16, 603–620.
- Mudie, P.J., Marret, F., Mertens, K.N., Shumilovskikh, L., Leroy, S.A.G., 2017. Atlas of modern dinoflagellate cyst distributions in the Black Sea Corridor: from Aegean to Aral Seas, including Marmara, Black, Azov and Caspian Seas. *Marine Micropaleontology* 134, 1–152.

- Narale, D.D., Naidu, P.D., Anil, A.C., Godad, S.P., 2015. Evolution of productivity and monsoonal dynamics in the eastern Arabian Sea during the past 68 ka using dinoflagellate cyst records. *Palaeogeography, Palaeoclimatology, Palaeoecology* 435, 193–202.
- Ndah, A.B., Becek, K., Dagar, L., 2016. A review of coastal upwelling research in the South China Sea: challenges, limitations and prospects. *International Journal of Earth and Atmospheric Science* 3, 63–72.
- Ning, X., Chai, F., Xue, H., Chai, Y., Liu, C., Shi, J., 2004. Physical-biological oceanographic coupling influencing phytoplankton and primary production in the South China Sea. *Journal of Geophysical Research* 109, C10005, doi:10.1029/2004JC002365.
- Pospelova, V., Head, M.J., 2002. *Islandinium brevispinosum* sp. nov. (Dinoflagellata), a new organic-walled dinoflagellate cyst from modern estuarine sediments of New England (USA). *Journal of Phycology* 38, 593–601.
- Pospelova, V., Kim, S.J., 2010. Dinoflagellate cysts in recent estuarine sediments from aquaculture sites of southern South Korea. *Marine Micropaleontology* 76, 37–51.
- Pospelova, V., Chmura, G.L., Boothman, W.S., Latimer, J.S., 2002. Dinoflagellate cyst records and human disturbance in two neighboring estuaries, New Bedford Harbor and Apponagansett Bay, Massachusetts (USA). *Science of the Total Environment* 298, 81–102.
- Pospelova, V., Chmura, G.L., Walker, H.A., 2004. Environmental factors influencing the spatial distribution of dinoflagellate cyst assemblages in shallow lagoons of southern New England (USA). *Review of Palaeobotany and Palynology* 128, 7–34.
- Pospelova, V., Chmura, G.L., Boothman, W.S., Latimer, J.S., 2005. Spatial distribution of modern dinoflagellate cysts in polluted estuarine sediments from Buzzards Bay (Massachusetts, USA) embayments. *Marine Ecology Progress Series* 292, 23–40.

- Pospelova, V., Pedersen, T.F., de Vernal, A., 2006. Dinoflagellate cysts as indicators of climatic and oceanographic changes during the past 40 kyr in the Santa Barbara Basin, southern California. *Paleoceanography* 21, PA2010, doi:10.1029/2005PA001251.
- Pospelova, V., de Vernal, A., Pedersen, T.F., 2008. Distribution of dinoflagellate cysts in surface sediments from the northeastern Pacific Ocean (43–25 degrees N) in relation to sea-surface temperature, salinity, productivity and coastal upwelling. *Marine Micropaleontology* 68, 21–48.
- Pospelova, V., Esenkulova, S., Johannessen, S.C., O'Brien, M.C., Macdonald, R.W., 2010. Organic-walled dinoflagellate cyst production, composition and flux from 1996 to 1998 in the central Strait of Georgia (BC, Canada). A sediment trap study. *Marine Micropaleontology* 75, 17-37.
- Pospelova, V., Price, A.M., Pedersen, T.F., 2015. Palynological evidence for late Quaternary climate and marine primary productivity changes along the California margin. *Paleoceanography* 30, 877–894.
- Price, A.M., Mertens, K.N., Pospelova, V., Pedersen, T.F., Ganeshram, R.S., 2013. Late Quaternary climatic and oceanographic changes in the Northeast Pacific as recorded by dinoflagellate cysts from Guaymas Basin, Gulf of California (Mexico). *Paleoceanography* 28, 200–212.
- Price, A.M., Pospelova, V., Coffin, M.R.S., Latimer, J.S., Chmura, G.L., 2016. Biogeography of dinoflagellate cysts in northwest Atlantic estuaries. *Ecology and Evolution* 6, 5648–5662.
- Qiu, Z., Jiang, H., Ding, L., Shang, X., 2020. Late pleistocene-Holocene vegetation history and anthropogenic activities deduced from pollen spectra and archaeological data at Guxu Lake, eastern china. *Nature* 10:109306, doi:10.1038/s41598-020-65834-z.

- Qu, T., 2002. Evidence for water exchange between the South China Sea and the Pacific Ocean through the Luzon Strait. *Acta Oceanologica Sinica* 21, 75–185.
- Qu, T., Girton, J.B., Whitehead, J.A., 2006. Deepwater overflow through Luzon Strait. *Journal of Geophysical Research* 111, C01002, doi:10.1029/2005jc003139.
- Radi, T., de Vernal, A., 2004. Dinocyst distribution in surface sediments from the northeastern Pacific margin (40–60 degrees N) in relation to hydrographic conditions, productivity and upwelling. *Review of Palaeobotany and Palynology* 128, 169–193.
- Radi, T., de Vernal, A., 2008a. Dinocysts as proxy of primary productivity in mid-high latitudes of the Northern Hemisphere. *Marine Micropaleontology* 68, 84–114.
- Radi, T., de Vernal, A., 2008b. Last glacial maximum (LGM) primary productivity in the northern North Atlantic Ocean. *Canadian Journal of Earth Sciences* 45, 1299–1316.
- Railsback, L.B., Liang, F.Y., Brook, G.A., Varrintsoa, N.R.G., Sletten, H.R., Marais, E., Hardt, B., Cheng, H., Edwards, R.L., 2013. The timing, two-pulsed nature, and variable climatic expression of the 4.2 ka event: A review and new high-resolution stalagmite data from Namibia. *Quaternary Science Reviews* 186, 78–90.
- Ran, M., Chen, L., 2019. The 4.2 ka BP climatic event and its cultural responses. *Quaternary International* 521, 153–167.
- Reichert, G.J., Brinkhuis, H., 2003. Late Quaternary *Protoperidinium* cysts as indicators of paleoproductivity in the northern Arabian Sea. *Marine Micropaleontology* 49, 303–315.
- Richerol, T., Rochon, A., Blasco, S., Scott, D.B., Schell, T.M., Bennett, R.J., 2008. Evolution of paleo sea-surface conditions over the last 600 years in the Mackenzie Trough, Beaufort Sea (Canada). *Marine Micropaleontology* 68, 6–20.

- Richerol, T., Rochon, A., Blasco, S., Scott, D.B., Schell, T.M., Bennett, R.J., 2008. Distribution of dinoflagellate cysts in surface sediments of the Mackenzie Shelf and Amundsen Gulf, Beaufort Sea (Canada). *Journal of Marine Systems* 74, 825–839.
- Richerol, T., Pienitz, R., Rochon, A., 2012. Modern dinoflagellate cyst assemblages in surface sediments of Nunatsiavut fjords (Labrador, Canada). *Marine Micropaleontology* 88–89, 54–64.
- Richerol, T., Pienitz, R., Rochon, A., 2014. Recent anthropogenic and climatic history of Nunatsiavut fjords (Labrador, Canada). *Paleoceanography* 29, 869–892.
- Richerol, T., Frechette, B., Rochon, A., Pienitz, R., 2016. Holocene climate history of the Nunatsiavut (northern Labrador, Canada) established from pollen and dinoflagellate cyst assemblages covering the past 7000 years. *Holocene* 26, 44–60.
- Richter, T.O., Van Der Gaast, S., Koster, L., Vaars, A., Gieles, R., De Stigter, H.C., De Haas, H., Van Weering, T.C.E., 2006. The Avaatech XRF Core Scanner: technical description and applications to NE Atlantic sediments. *New Techniques in Sediment Core Analysis* 267, 39–50.
- Rochon, A., De Vernal, A., 1994. Palynomorph Distribution in Recent Sediments from the Labrador Sea. *Canadian Journal of Earth Sciences* 31, 115–127.
- Rochon, A., de Vernal, A., Sejrup, H.P., Haflidason, H., 1998. Palynological evidence of climatic and oceanographic changes in the North Sea during the last deglaciation. *Quaternary Research* 49, 197–207.
- Rochon, A., de Vernal, A., Turon, J.-L., Matthiessen, J., Head, M.J., 1999. Distribution of recent dinoflagellate cysts in surface sediments from the North Atlantic Ocean and adjacent areas

- in relation to sea-surface parameters. In: American Association of Stratigraphic Palynologists, Contributions Series 35, pp. 146–152.
- Shao, L., Li, X.J., Geng, J.H., Pang, X., Lei, Y.C., Qiao, P.J., Wang, L.L., Wang, H.B., 2007. Deep water bottom current deposition in the northern South China Sea. *Science in China Series D-Earth Sciences* 50, 1060–1066.
- Shaw, P.-T., 1996. Winter upwelling off Luzon in the northeastern South China. *J. Geophys. Res.* 101, 16435–16448.
- Sheng, M., Wang, X., Zhang, S., Chu, G., Su, Y., Yang, Z., 2017. A 20,000-year high-resolution pollen record from Huguangyan Maar Lake in tropical–subtropical South China. *Palaeogeography, Palaeoclimatology, Palaeoecology* 472, 83–92.
- Shintani, T., Yamamoto, M., Chen, M.-T., 2011. Palaeoenvironmental changes in the northern South China Sea over the past 28,000 years: A study of TEX86-derived sea surface temperatures and terrestrial biomarkers. *Journal of Asian Earth Sciences* 40, 1221–1229.
- Solignac, S., Giraudeau, J., de Vernal, A., 2006. Holocene sea surface conditions in the western North Atlantic: Spatial and temporal heterogeneities. *Paleoceanography* 21, PA2004, doi:10.1029/2005PA001175.
- Spengler III, R.N., Ryabogina, N., Tarasov, P.E., Wagner, M., 2016. The spread of agriculture into northern Central Asia: Timing, pathways, and environmental feedbacks. *The Holocene* 26, 1527–1540.
- Steinke, S., Glatz, C., Mohtadi, M., Groeneveld, J., Li, Q., Jian, Z., 2011. Past dynamics of the East Asian monsoon: No inverse behaviour between the summer and winter monsoon during the Holocene. *Global and Planetary Change* 78, 170–177.

- Stevens, C.J., Murphy, C., Roberts, R., Lucas, L., Silva, F., Fuller, D.Q., 2016. Between China and South Asia: A Middle Asian corridor of crop dispersal and agricultural innovation in the Bronze Age. *Holocene* 26, 1541–1555.
- Taira, K., 1975. Holocene crustal movements in Taiwan as indicated by radiocarbon dating of marine fossils and driftwood. *Tectonophysics* 28, T1–T5, doi:10.1016/0040-1951(75)90057-8.
- Tanabe, S., Saito, Y., Lan Vu, Q., Hanebuth, T.J.J., Lan Ngo, Q., Kitamura, A., 2006. Holocene evolution of the Song Hong (Red River) delta system, northern Vietnam. *Sedimentary Geology* 187, 29–61.
- Telford, R.J., Birks, H.J.B., 2011. QSR Correspondence “Is spatial autocorrelation introducing biases in the apparent accuracy of palaeoclimatic reconstructions?” *Quaternary Science Reviews* 30, 3210–3213.
- ter Braak, C.J.F., Šmilauer, P., 2002. *CANOCO reference manual and CanoDraw for Windows user's guide. Software for Canonical Community Ordination (Version 4.5)*. Microcomputer Power, Ithaca, New York, p. 500.
- Tjallingii, R., Rohl, U., Kelling, M., Bickert, T., 2007. Influence of the water content on X-ray fluorescence core scanning measurements in soft marine sediments, *Geochemistry, Geophysics, Geosystems* 8, Q02004, doi:10.1029/2006GC001393.
- Uddandam, P.R., Prasad, V., Manoj, M.C., 2020. New dinoflagellate cysts from the recent sediments of northern Indian Ocean. *Journal of the Palaeontological Society of India* Volume 65, 15–26.
- Ujiie, Y., Ujiie, H., Taira, A., Nakamura, T., Oguri, K., 2003. Spatial and temporal variability of surface water in the Kuroshio source region, Pacific Ocean, over

- the past 21,000 years: evidence from planktonic foraminifera. *Marine Micropaleontology* 49, 335–364.
- Van Nieuwenhove, N., Pearce, C., Knudsen, M.F., Roy, H., Seidenkrantz, M.S., 2018. Meltwater and seasonality influence on Subpolar Gyre circulation during the Holocene. *Palaeogeography, Palaeoclimatology, Palaeoecology* 502, 104–118.
- Van Nieuwenhove, N., Head, M.J., Limoges, A., Pospelova, V., Mertens, K.N., Matthiessen, J., De Schepper, S., De Vernal, A., Eynaud, F., Londeix, L., Marret, F., Penaud, A., Radi, T., Rochon, A., 2020. An overview and brief description of common marine organic-walled dinoflagellate cyst taxa occurring in surface sediments of the Northern Hemisphere. *Marine Micropaleontology* 159, 101814, doi:10.1016/j.micropaleo.2019.101814.
- Verleye, T.J., Louwye, S., 2010. Recent geographical distribution of organic-walled dinoflagellate cysts in the southeast Pacific (25–53°S) and their relation to the prevailing hydrographical conditions. *Palaeogeography, Palaeoclimatology, Palaeoecology* 298, 319–340.
- Verleye, T.J., Mertens, K.N., Louwye, S., Arz, H.W., 2009. Holocene Salinity Changes in the Southwestern Black Sea: A Reconstruction Based on Dinoflagellate Cysts. *Palynology* 33, 77–100.
- Verleye, T.J., Pospelova, V., Mertens, K.N., Louwye, S., 2011. The geographical distribution and (palaeo)ecology of *Selenopemphix undulata* sp. nov., a new late Quaternary dinoflagellate cyst from the Pacific Ocean. *Marine Micropaleontology* 78, 65–83.
- Wall, D., Dale, B., Lohmann, G.P., Smith, W.K., 1977. Environmental and Climatic Distribution of Dinoflagellate Cysts in Modern Marine-Sediments from Regions in North and South-Atlantic Oceans and Adjacent Seas. *Marine Micropaleontology* 2, 121–200.

- Wang, H., Wang, Y., Qiu, Y., Peng, X., Liu, Y., 2008. Geomorphology and its control of deep water slope of the margin of the South China Sea. *Acta Oceanologica Sinica* 30, 70–79.
- Wang, L., Sarnthein, M., Erlenkeuser, H., Grimalt, J., Grootes, P., Heilig, S., Ivanova, E., Kienast, M., Pelejero, C., Pflaumann, U., 1999. East Asian monsoon climate during the Late Pleistocene: high-resolution sediment records from the South China Sea. *Marine Geology* 156, 245–284.
- Wang, L., Sarnthein, M., Erlenkeuser, H., Grootes, P.M., Grimalt, J.O., Pelejero, C., Linck, G., 1999. Holocene variations in Asian monsoon moisture: a bi-decadal sediment record from the South China Sea. *Geophysical Research Letters* 26, 2889–2892.
- Wang, P., Li, Q., 2009. *The South China Sea: Paleogeography and Sedimentology*. Springer Press, pp. 1–6.
- Wang, X., Chen, F., Zhang, J., Yang, Y., Li, J., Hasi, E., Zhang, C., Xia, D., 2010. Climate, desertification, and the rise and collapse of China's historical dynasties. *Human Ecology* 38, 157–172.
- Wang, Y.J., Cheng, H., Edwards, R.L., He, Y., Kong, X., An, Z., Wu, J., Kelly, M.J., Dykoski, C.A., Li, X., 2005. The Holocene Asian monsoon: Links to solar changes and North Atlantic climate. *Science* 308, 854–857.
- Wei, G., Deng, W., Yu, K., Li, X., Sun, W., Zhao, J., 2007. Sea surface temperature records in the northern South China Sea from mid-Holocene coral Sr/Ca ratios. *Paleoceanography* 22, PA3206.
- Wei, K., Yang, T., Huang, C., 1997. Glacial-Holocene calcareous nannofossils and paleoceanography in the northern South China Sea. *Marine Micropaleontology* 32, 95–114.

- Woodruff, J.D., Donnelly, J.P., Okusu, A., 2009. Exploring typhoon variability over the mid-to-late Holocene: evidence of extreme coastal flooding from Kamikoshiki, Japan. *Quaternary Science Reviews* 28, 1774–1785.
- Wu, C.-R., Hsin, Y.-C., 2012. The forcing mechanism leading to the Kuroshio intrusion into the South China Sea. *Journal of Geophysical Research* 117, C07015, doi:10.1029/2012JC007968.
- Wu, M.-S., Zong, Y., Mok, K.-M., Cheung, K.-M., Xiong, H., Huang, G., 2017. Holocene hydrological and sea surface temperature changes in the northern coast of the South China Sea. *Journal of Asian Earth Sciences* 135, 268–280.
- Xia, P., Meng, X., Li, Z., Zhi, P., Zhao, M., Wang, E., 2019. Late Holocene mangrove development and response to sea level change in the northwestern South China Sea. *Acta Oceanologica Sinica* 38, 111–120.
- Xiao, J., Zhang, S., Fan, J., Wen, R., Zhai, D., Tian, Z., Jiang, D., 2018. The 4.2 ka BP event: multi-proxy records from a closed lake in the northern margin of the East Asian summer monsoon. *Climate of the Past* 14, 1417–1425.
- Xie, S., Xie, Q., Wang, D., Liu, W., 2003. Summer upwelling in the South China Sea and its role in regional climate variations. *Journal of Geophysical Research-Oceans* 108, C8 3261, doi:10.1029/2003JC001867, 2003.
- Xiong, H., Zong, Y., Huang, G., Fu, S., 2018a. Sedimentary responses to Holocene sea-level change in a shallow marine environment of southern China. *Journal of Asian Earth Sciences* 166, 95–106.
- Xiong, H., Zong, Y., Qian, P., Huang, G., Fu, S., 2018b. Holocene sea-level history of the northern coast of South China Sea. *Quaternary Science Reviews* 194, 12–26.

- Xu, F., Hu, B., Dou, Y., Liu, X., Wan, S., Xu, Z., Tian, X., Liu, Z., Yin, X., Li, A., 2017. Sediment provenance and paleoenvironmental changes in the northwestern shelf mud area of the South China Sea since the mid-Holocene. *Continental Shelf Research* 144, 21–30.
- Yan, H., Soon, W., Wang, Y., 2015. A composite sea surface temperature record of the northern South China Sea for the past 2500 years: A unique look into seasonality and seasonal climate changes during warm and cold periods. *Earth-Science Reviews* 141, 122–135.
- Yan, H., Sun, L.G., Shao, D., Wang, Y.H., 2015. Seawater temperature seasonality in the South China Sea during the late Holocene derived from high-resolution Sr/Ca ratios of *Tridacna gigas*. *Quaternary Research* 83, 298–306.
- Yan, M., Liu, J., 2019. Physical processes of cooling and mega-drought during the 4.2 ka BP event: results from TraCE-21ka simulations. *Climate of the Past* 15, 265–277.
- Yao, A., 2008. Culture contact and social change along China's ancient southwestern frontier, 900 B.C.--100 A.D. Ph.D Dissertation, University of Michigan.
- Yao, A., Jiang, Z., 2012. Rediscovering the settlement system of the 'Dian' kingdom, in Bronze Age southern China. *Antiquity* 85, 353–367.
- Yim, W.W.S., Huang, G., 2022. Middle Holocene higher sea-level indicators from the south China coast. *Marine Geology* 182, 225–230.
- Yu, K., Zhao, J., Wei, G., Cheng, X., Wang, P., 2005. Mid-late Holocene monsoon climate retrieved from seasonal Sr/Ca and delta O-18 records of *Porites lutea* corals at Leizhou Peninsula, northern coast of South China Sea. *Global and Planetary Change* 47, 301–316.
- Yuan, Y., Zhao, J., Wang, H., Lou, R., Chen, H., Wang, K., 2002. Current measurements and spectral analyses in the upper 450 m and deep layers of the northeastern South China Sea. *Science China Series D* 45, 1008–1027.

- Yue, Y., Zheng, Z., Rolett, B.V., Ma, T., Chen, C., Huang, K., Lin, G., Zhu, G., Cheddadi, R., 2015. Holocene vegetation, environment and anthropogenic influence in the Fuzhou Basin, southeast China. *Journal of Asian Earth Sciences* 99, 85–94.
- Zhang, H., Liu, C., Jin, X., Shi, J., Zhao, S., Jian, Z., 2016. Dynamics of primary productivity in the northern South China Sea over the past 24,000 years. *Geochemistry, Geophysics, Geosystems* 17, 4878–4891.
- Zhang, P., Cheng, H., Edwards, R.L., Chen, F., Wang, Y., Yang, X., Liu, J., Tan, M., Wang, X., Liu, J., An, C., Dai, Z., Zhou, J., Zhang, D., Jia, J., Jin, L., Johnson, K.R., 2008. A Test of Climate, Sun, and Culture Relationships from an 1816-Year Chinese Cave Record. *Science* 322, 940–942.
- Zhao, L., Ma, C., Leipe, C., Long, T., Liu, K.-P., Ju, H., Tang, L., Zhang, Y., Wagner, M., Tarasov, P.E., 2017. Holocene vegetation dynamics in response to climate change and human activities derived from pollen and charcoal records from southeastern China. *Palaeogeography, Palaeoclimatology, Palaeoecology* 485, 644–660.
- Zhao, J., Yu, K., 2002. Timing of Holocene sea-level highstands by mass spectrometric U-series ages of a coral reef from Leizhou Peninsula, South China Sea. *Chinese Science Bulletin* 47, 348–352.
- Zhao, X., Dupont, L., Schefuss, E., Granger, R., Wefer, G., 2019. Late-Holocene oceanic variability in the southern Benguela region driven by interplay of upwelling, fluvial discharge, and Agulhas leakage. *Holocene* 29, 219–230.
- Zhao, Y., Liu, Z., Zhang, Y., Li, J., Wang, M., Wang, W., Xu, J., 2015. In situ observation of contour currents in the northern South China Sea: Applications for deepwater sediment transport. *Earth and Planetary Science Letters* 430, 477–485.

- Zhao, Y., Morzadec-Kerfourn, M.T., 1992a. Late Pleistocene-Holocene dinoflagellate cysts from the South China Sea. *Acta Micropalaeontologica Sinica* 9 (3), 291–302 [in Chinese with English abstract].
- Zhao, Y., Morzadec-Kerfourn, M.T., 1992b. Dinoflagellate cysts, pollen and spores in Quaternary sediments of the abyssal basin of the South China Sea: their palaeoenvironmental significance. *Review of Micropaleontology* 35, 77–88 [in French with English abstract].
- Zhao, Y., Morzadec-Kerfourn, M.T., 1994. Two new dinoflagellate cysts: *Spiniferites pacificus* nov. sp. et *Pentadinium netangei* nov. sp., from the Pleistocene of the North- West Pacific. *Geobios* 27, 261–269 [in French with English abstract].
- Zhou, L., Yang, Y., Wane, Z., Jia, J., Mao, L., Li, L., Fang, X., Gao, S., 2019. Investigating ENSO and WPWP modulated typhoon variability in the South China Sea during the mid-late Holocene using sedimentological evidence from southeastern Hainan Island, China. *Marine Geology* 416, doi:10.1016/j.margeo.2019.105987.
- Ziegler, M., Jilbert, T., de Lange, G.J., Lourens, L.J., Reichert, G.J., 2008. Bromine counts from XRF scanning as an estimate of the marine organic carbon content of sediment cores. *Geochemistry, Geophysics, Geosystems* 9, Q05009, doi:10.1029/2007GC001932.
- Zong, Y., 2004. Mid-Holocene sea-level highstand along the Southeast Coast of China. *Quaternary International* 117, 55–67.
- Zong, Y., Huang, G., Switzer, A.D., Yu, F., Yim, W.W-S., 2009. An evolutionary model for the Holocene formation of the Pearl River delta, China. *The Holocene* 19, 129–142.

- Zonneveld, K.A.F., 1996. Palaeoclimatic reconstruction of the last deglaciation (18–8 ka BP) in the Adriatic Sea region; A land-sea correlation based on palynological evidence. *Palaeogeography, Palaeoclimatology, Palaeoecology* 122, 89–106.
- Zonneveld, K.A.F., 1997. Dinoflagellate cyst distribution in surface sediments from the Arabian Sea (northwestern Indian Ocean) in relation to temperature and salinity gradients in the upper water column. *Deep-Sea Research Part II-Topical Studies in Oceanography* 44, 1411–1443.
- Zonneveld, K.A.F., Ganssen, G., Troelstra, S., Versteegh, G.J.M., Visscher, H., 1997. Mechanisms forcing abrupt fluctuations of the Indian Ocean summer monsoon during the last deglaciation. *Quaternary Science Reviews* 16, 187–201.
- Zonneveld, K.A.F., Marret, F., Versteegh, G.J.M., Bogus, K., Bonnet, S., Bouimtarhan, I., Crouch, E., de Vernal, A., Elshanawawy, K., Edwards, L., Esper, O., Forke, S., Grøsfjeld, K., Henry, M., Holzwarth, U., Kieft, J.-F., Kim, S.-Y., Ladouceur, S., Ledu, D., Chen, L., Limoges, A., Londeix, L., Lu, S.H., Mahmoud, M.S., Marino, G., Matsouka, K., Matthiessen, J., Mildenhall, D.C., Mudie, P., Neil, H.L., Pospelova, V., Qi, Y., Radi, T., Richerol, T., Rochon, A., Sangiorgi, F., Solignac, S., Turon, J.-L., Verleye, T., Wang, Y., Wang, Z., Young, M., 2013. Atlas of modern dinoflagellate cyst distribution based on 2405 data points. *Review of Palaeobotany and Palynology* 191, 1–197.
- Zonneveld, K.A.F., Pospelova, V., 2015. A determination key for modern dinoflagellate cysts. *Palynology* 39, 387–409.
- Zonneveld, K.A.F., Susek, E., Fischer, G., 2010. Seasonal variability of the organic-walled dinoflagellate cyst production in the coastal upwelling region off Cape Blanc (Mauritania): a five-year survey. *Journal of Phycology* 46, 202–215.

## List of Figures and Tables

Fig. 1. (a) Inset: The study area (orange square) and the locations of 398 sites used to compile the North Pacific dinoflagellate cyst database (sites from de Vernal et al. (2020) are in blue and Li et al. (2020) are in red); (b) Geographic map of the northern South China Sea showing bathymetric features and the location of sediment core GLW31D (this study, red triangle). White triangles indicate locations of Dongge cave ('Dongge' on map; Wang et al., 2005) and other sediment cores: HKVU11 (Wu et al., 2017), NS02G (Kong et al., 2014), MD05–2904 (Steinke et al., 2011), MD97–2146 (Shintani et al., 2011) and 17940 (Jiang et al., 2014). The red dashed line marks the general route of the deep water current.

Fig. 2. Sea-surface temperature (SST) and sea-surface salinity (SSS) of the South China Sea in February and August (modified from <http://marine.copernicus.eu>).

Fig. 3. Surface currents and primary productivity (PP) of the South China Sea in February and August. White arrow lines show current directions (modified from <http://marine.copernicus.eu>; Fang et al., 1998; Qu et al., 2002; Li et al., 2020).

Fig. 4. Age-depth relationship of core GLW31D shown by the calibrated dates plotted against sediment depth. Underlined numbers are the sedimentation rates ( $\text{cm kyr}^{-1}$ ) calculated by linear interpolation between two adjacent  $^{14}\text{C}$  ages. The horizontal red bars of each points show the 95% confidence intervals of ages, and vertical red bars show 2-cm sediment thickness for each point.

Fig. 5. Sediment components and ratios of geochemical elements (Si, Fe, Ba, and K) to Al of core GLW31D over the last 12,500 years.

Fig. 6. Relative abundances (%) and concentrations ( $\times 10^2$  cysts  $g^{-1}$ ) of selected dinoflagellate cyst taxa from core GLW31D. The color bands and dashed lines across the figure show dinoflagellate cyst zones and subzones (DIa to DVc). Zonation is determined by constrained cluster analysis (CONISS) of relative abundances of dinoflagellate cysts.

Fig. 7. Ordination diagram generated by principal component analysis (PCA) of dinoflagellate cyst percentages in core GLW31D. Purple squares, green diamonds, red triangles, blue open circles and orange filled circles corresponding samples from dinoflagellate cyst zones DI to DV, respectively, as shown in Fig.5.

Fig. 8. The results of the validation exercise showing estimated values using modern analogue technique vs. observed data of oceanographic parameters (SST-Feb: sea-surface temperature in February; SST-Aug: sea-surface temperature in August; SSS-Feb: sea-surface salinity in February; SSS-Aug: sea-surface salinity in August; PP-Feb: primary productivity in February; PP-Aug: primary productivity in August; PP-An: annual primary productivity).  $R^2$  is a coefficient of determination and SD is the standard deviation

Fig. 9. Dinoflagellate cyst-based reconstructions of SST, SSS and PP for core GLW31D and regional relative sea-level changes over the last 12,500 years. a. SST-Feb: sea-surface

temperature in February; b. SST-Aug: sea-surface temperature in August; c. SSS-Feb: sea-surface salinity in February; d. SSS-Aug: sea-surface salinity in August; e. PP-Feb: primary productivity in February; f. PP-Aug: primary productivity in August; g. PP-An: annual primary productivity; h. sea-level curves. The solid lines on the inserts 7a–g correspond to the best estimates of the reconstructed parameters, and the light gray lines show error bars. The black lines in a–b, and the red lines in 7c–g are smoothed curves. The gray bar highlights stage I of the sea-level rise before 7000 (or 6800) cal yr BP. The dash line separates the decelerated sea-level rise (Ib) from the rapid sea-level rise (Ia). The red marked the sea level stage II characterized by a highstand and the warmest climate, followed by stage III with a slight sea-level fall. The blue bar marks an abrupt cooling and dry interval characterized by high PP at ~2700–2400 cal yr BP.

Fig. 10. Comparison of previously published and this study reconstructed SST and SSS results for the northern South China Sea and adjacent areas over the last 7000 years. The blue bars mark the cooling event at ~2700–2400 cal yr BP in our study and the regional cooling event at 4.0 ka (not identified in our study). The red bar indicates the warmest period. Locations of Dongge cave (Wang et al., 2005) and sediment cores of HKVU11 (Wu et al., 2017), NS02G (Kong et al., 2014), MD05-2904 (Stenke et al., 2011), MD97-2146 (Shintani et al., 2011) and 17940 (Jiang et al., 2014) are shown on the map in Fig. 1.

Fig. 11. Downcore profiles of the reconstructed SST, SSS, PP as well as the ratios of heterotrophic to autotrophic dinoflagellates, silicon (Si/Al), iron (Fe/Al), and barium (Ba/Al) over the last 3200 years in core GLW31D. On the left, the diagram illustrates the duration of Chinese dynasties. The number of 1-24 labels the dynasties or state periods from 1–2. Xia

(2070–1600 BC) and Shang (1600–1027 BC) throughout to 24. Qing (1644–1911) in chronological order. Two intervals, highlighted in grey color (~2700–2400 cal yr BP and ~1000–600 cal yr BP), correspond to the split states of Chinese dynasty in 770–221 BC, including dynasties of 4. Eastern Zhou (770–221 BC), 5. Spring and Autumn Period (770–476 BC) and 6. Warring States Period (476–221 BC), and AD 907–1368 involving 17. Five Dynasties Period (907–960), 18. Liao (916–1125), 19. Northern Song (960–1125), 20. Jin (1115–1234), 21. Southern Song (1127–1279), and 22. Yuan (1279–1368). On the right, the regional climate records from other publications are shown: a. Jinggang (Huang et al., 2014), b. Dongge Cave (Dykoski et al., 2005; Wang et al., 2005), c. Song Hong (Red River) Delta (Li et al., 2006), d. Huguangyan Maar Lake (Sheng et al., 2017), e. Pearl estuary (Yang et al., 2010), f. Pearl Estuary (Kong et al., 2014), g. Fujian Basin (Yue et al., 2014), h. Jianfei Cave, Taiwan (Li et al., 2015), i. Paoay Lake, the Philippines (Son et al., 2016), j. MD05–2906 (Dai and Weng, 2015), k. Core 17940 (Jiang et al., 2014), l. Core NS02G (Kong et al., 2014), m. Xiasha and Leizhou Peninsula (Yu et al., 2005; Yan et al., 2014), n. Gulf of Tonkin (Beibuwan) (Li et al., 2010).

Plate I. 1-4. *Cryodinium?* spp. 1. UVic14-75-1, 1a: upper focus on apex view; 1b: outline and high septa; 1c: lower focus on antipex view; 2. UVic14-85-1, 2a: upper focus; 2b: high septa; 2c: lower focus on archeopyle; 3. UVic15-198-1, 3a: upper focus on apex view; 3b: high septa; 3c: lower focus; 4. UVic14-76—1, 4a: upper focus on apex view; 4b: high septa; 4c: lower focus. The Scale bars are 10  $\mu\text{m}$ .

### Supplementary materials

Fig. S1. Ordination diagrams of Canonical Correspondence Analysis (CCA) performed on logarithmically transformed dinoflagellate cyst relative abundances in surface sediments from the compiled North Pacific database and observed environmental parameters. SST-Feb: mean sea surface temperature in February; SST-Aug: mean sea-surface temperature in August; SSS-Feb: mean sea-surface salinity in February; SSS-Aug: mean sea-surface salinity in August; PP-Feb: mean primary productivity in February; PP-Aug: mean primary productivity in August; PP-An: mean annual primary productivity. Ordination diagram showing species scores (a) and sample scores (b). Marginal effects, conditional effects and summary of CCA axes statistics are shown as well. *P*-values < 0.05 are statistically significant and highlighted in bold. Lambda (A) is the variation explained by each environmental variable, considered independently (marginal effect), or considered after all variables already incorporated in the model (conditional effect). Red lines with arrows represent environmental variables.

Table S1. Names of dinoflagellate cyst taxa used for quantitative estimates and their abbreviations.

Table S2. Relative abundances of selected dinoflagellate cysts in surface sediments from the northern Pacific Ocean (Li et al., 2020; de Vernal et al., 2020) in modern analogue technical model. The full dinoflagellate cyst names and their abbreviations are listed in Table S1.

Table S3. Sample locations (coordinates and water depths) of modern dinoflagellate cyst dataset of the northern Pacific Ocean and sea-surface temperature, salinity and primary productivity of the sample sites (Li et al., 2020; de Vernal et al., 2020).

Table S4. Comparison of coefficients and standard deviations of estimated monthly SSS, SST, and PP from models of MAT (including WMAT) and WAPLS correlated with observation data.

Table S5. Dinoflagellate cyst relative abundances (percentages) in core GLW31D. The full dinoflagellate cyst names and their abbreviations are listed in Table S2.

Journal Pre-proof

## Highlights

- It contributes the first dinocyst-based quantitative reconstruction in the western Pacific.
- Taiwan Strait might open at ~9900 cal yr BP, showed by a decrease in *Impagidinium*.
- The warmest water in the northern South China Sea was in ~6800-5500 cal yr BP.
- A cold event at ~2700–2400 cal yr BP was identified.
- Human activities partially contributed to the high PP events in the late Holocene.

Journal Pre-proof

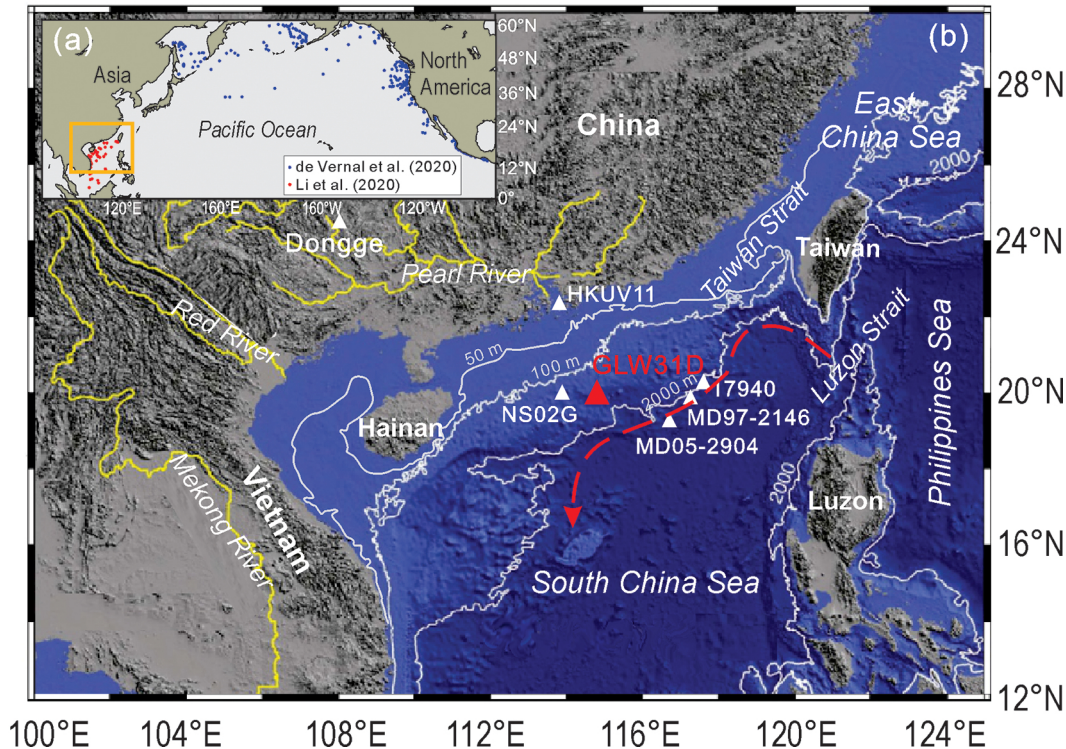


Figure 1

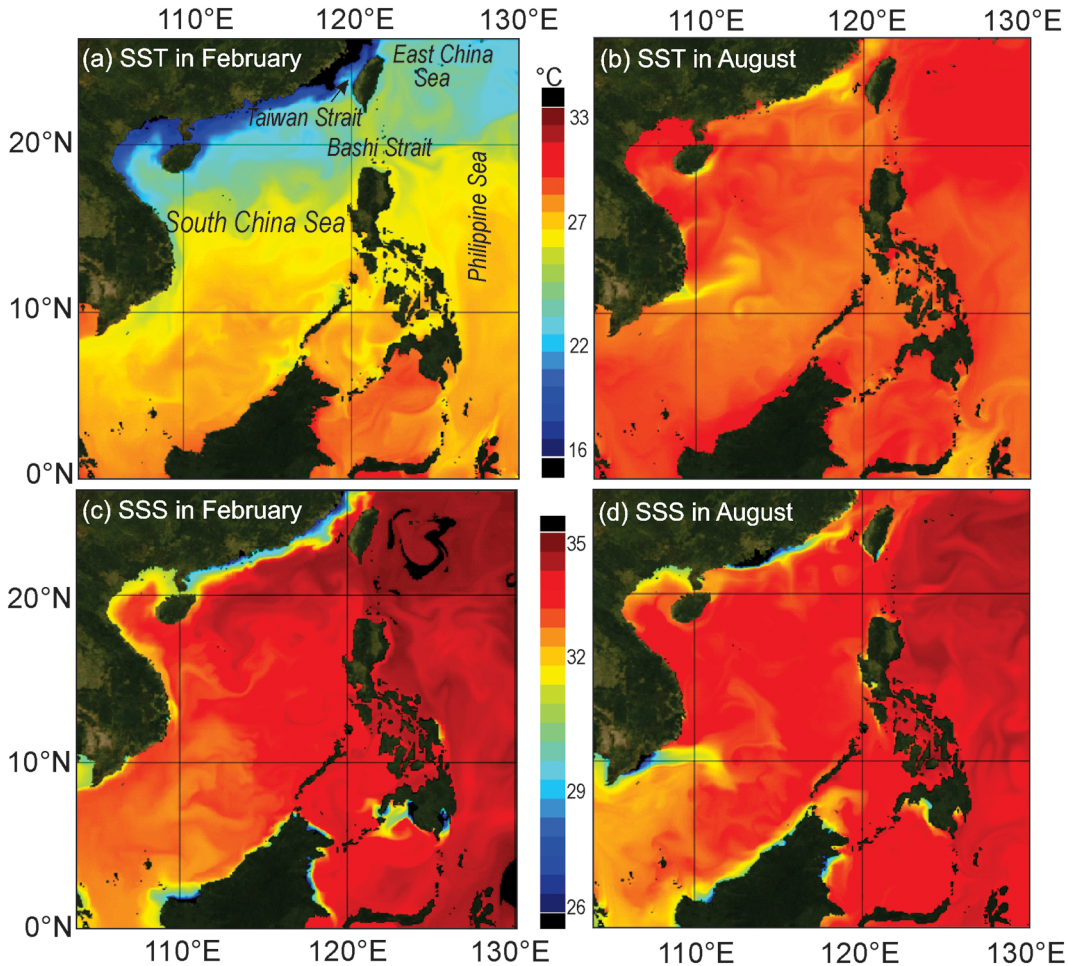


Figure 2

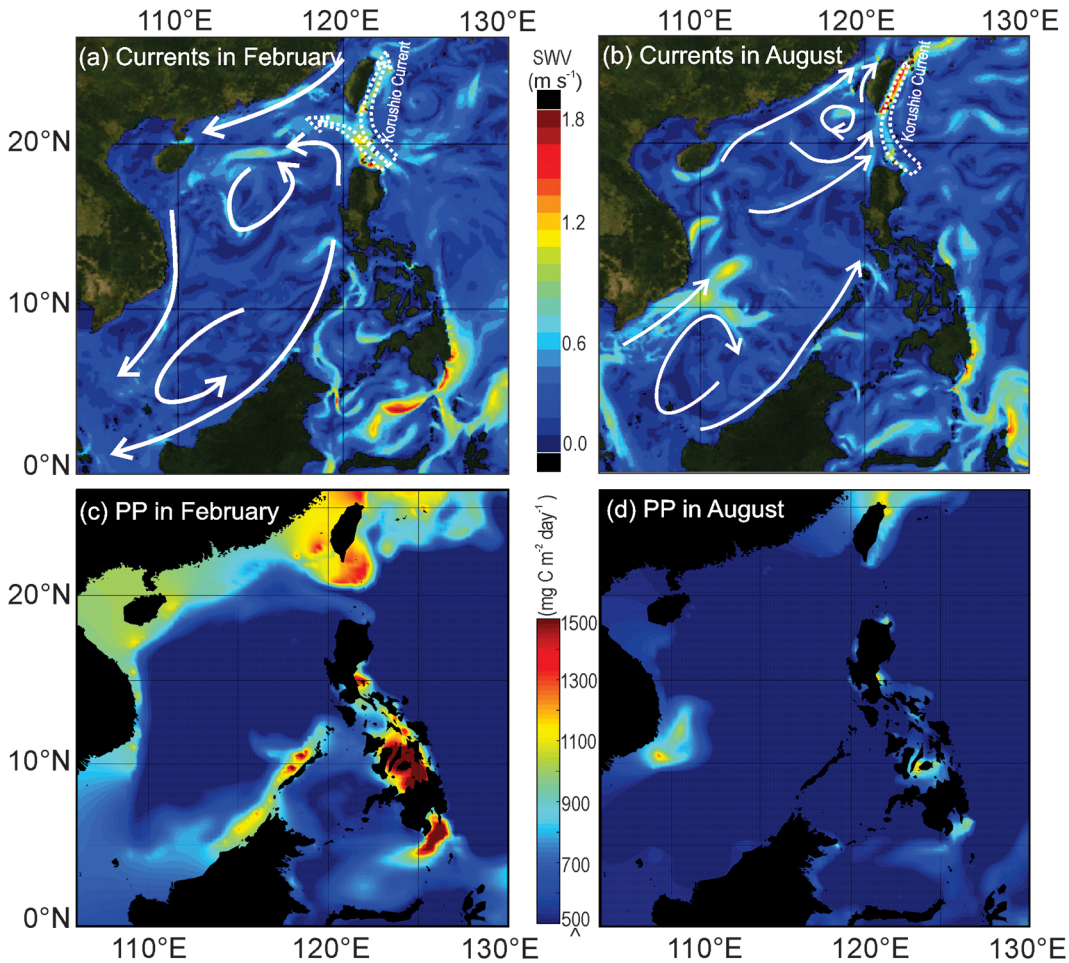


Figure 3

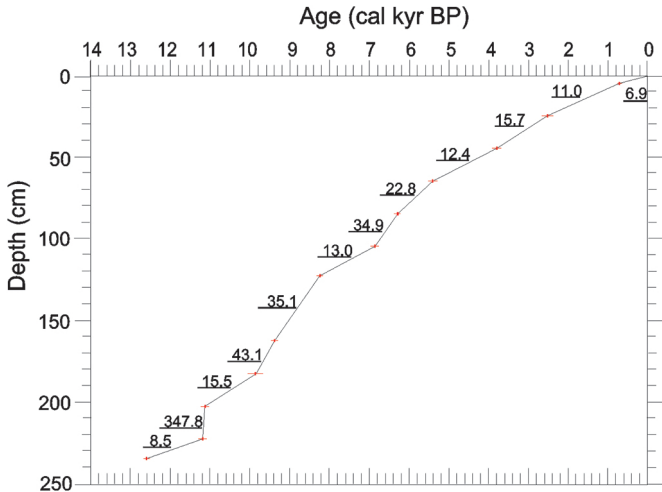


Figure 4

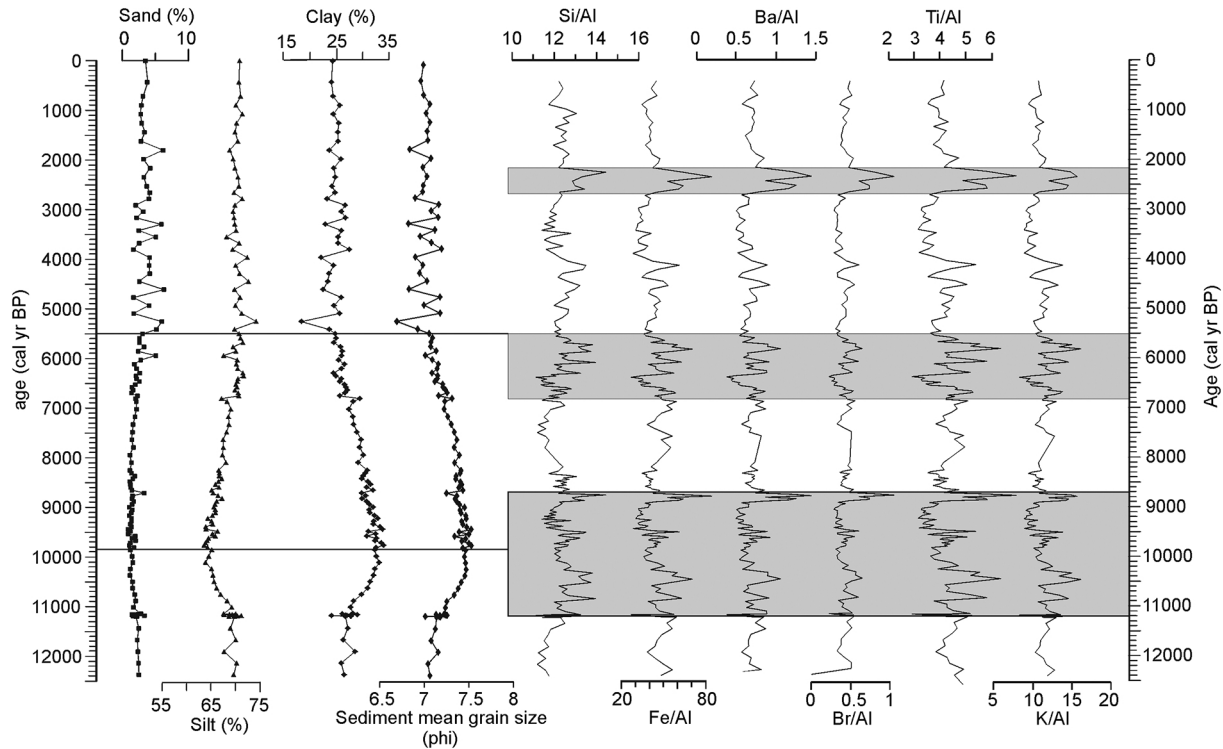


Figure 5

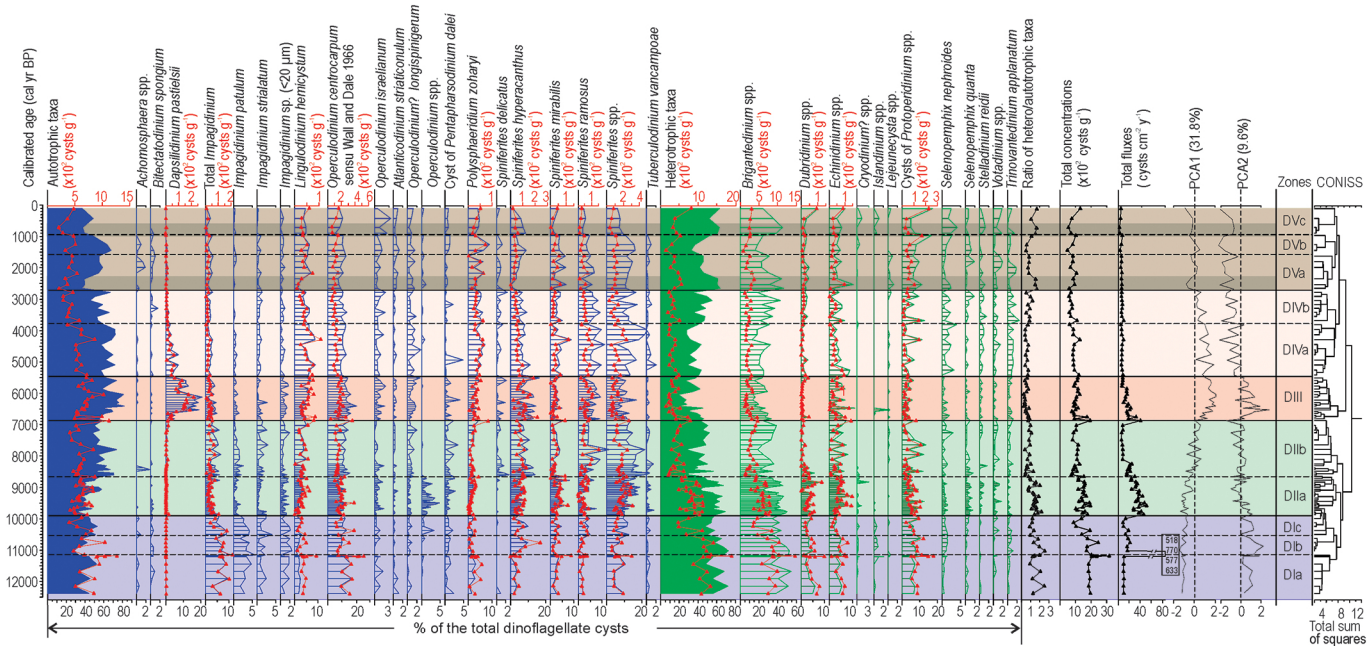


Figure 6

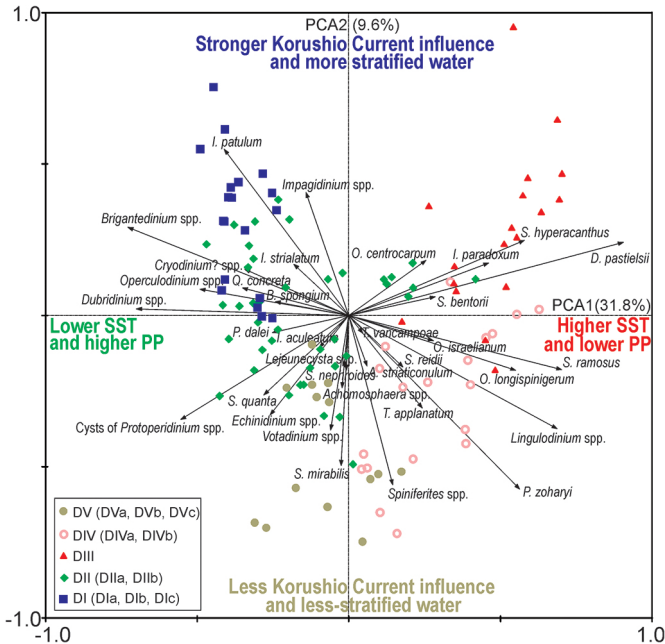


Figure 7

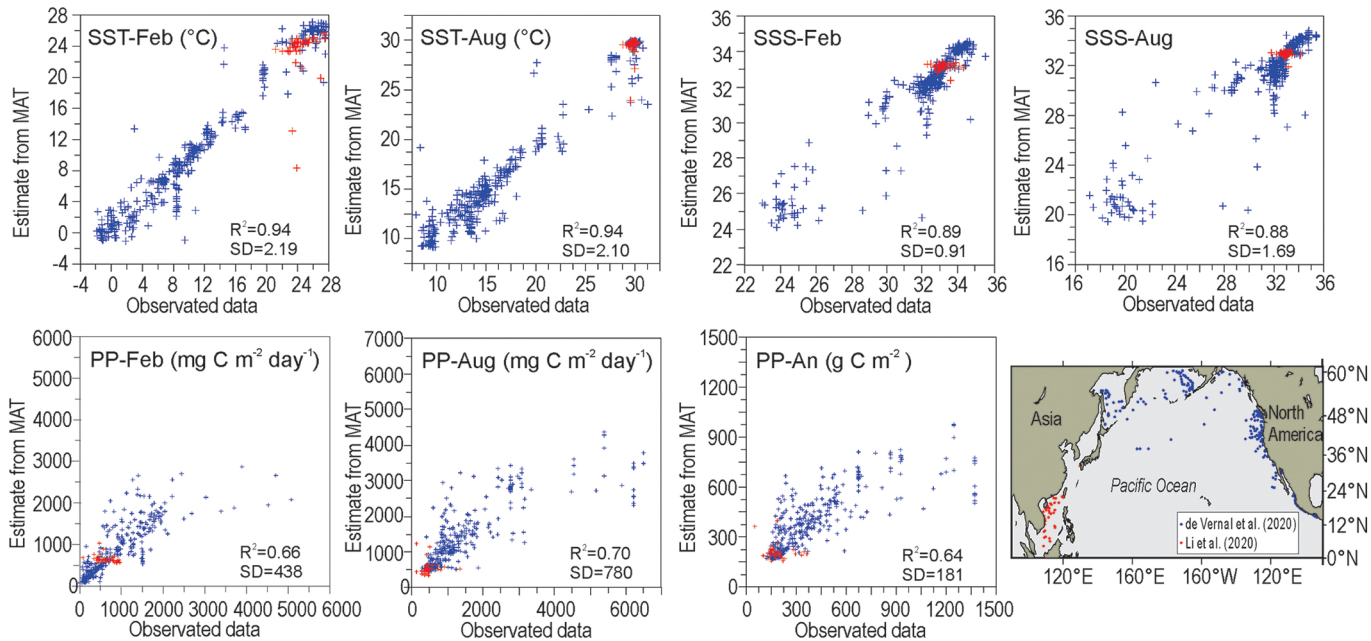


Figure 8

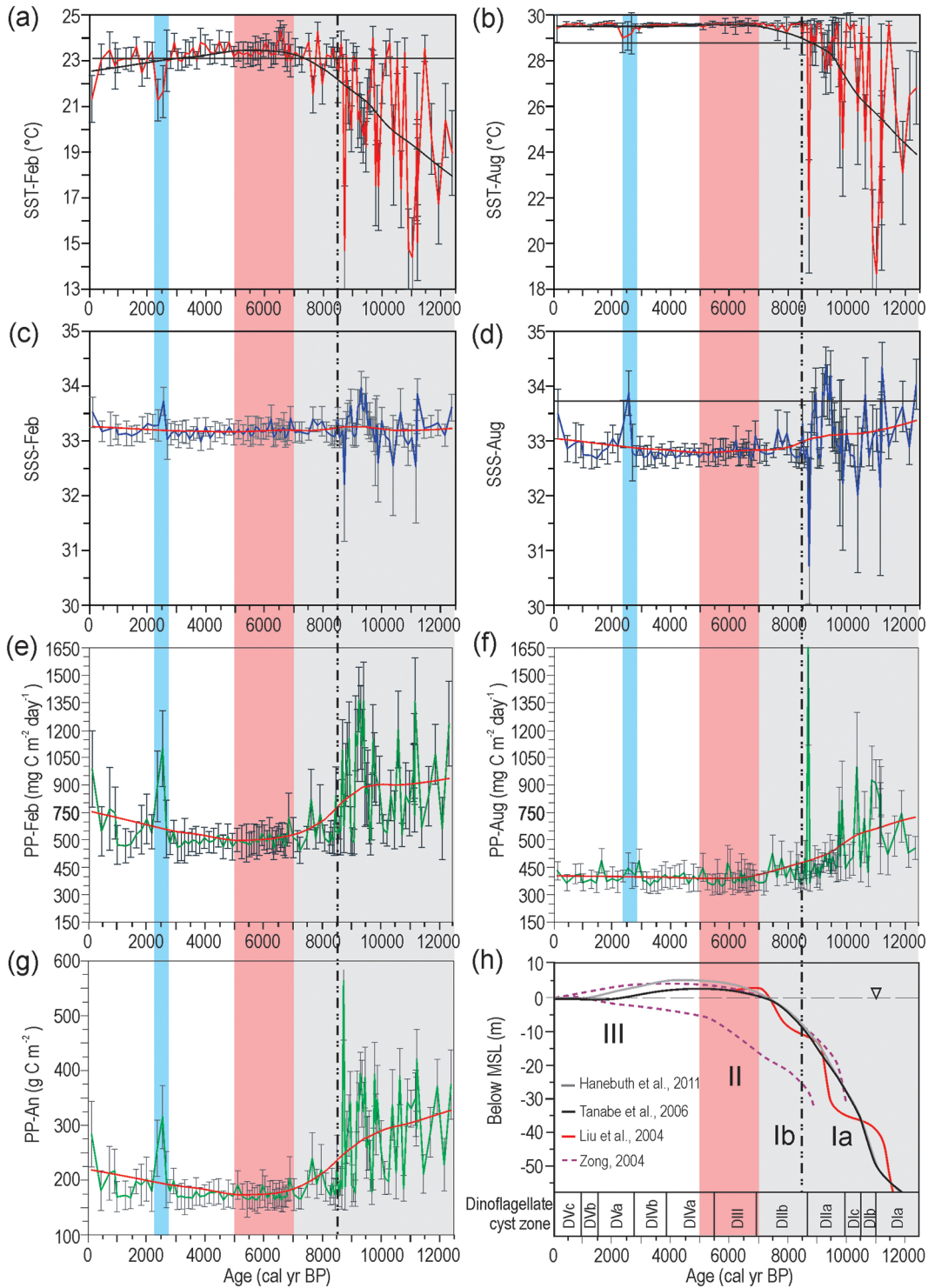


Figure 9

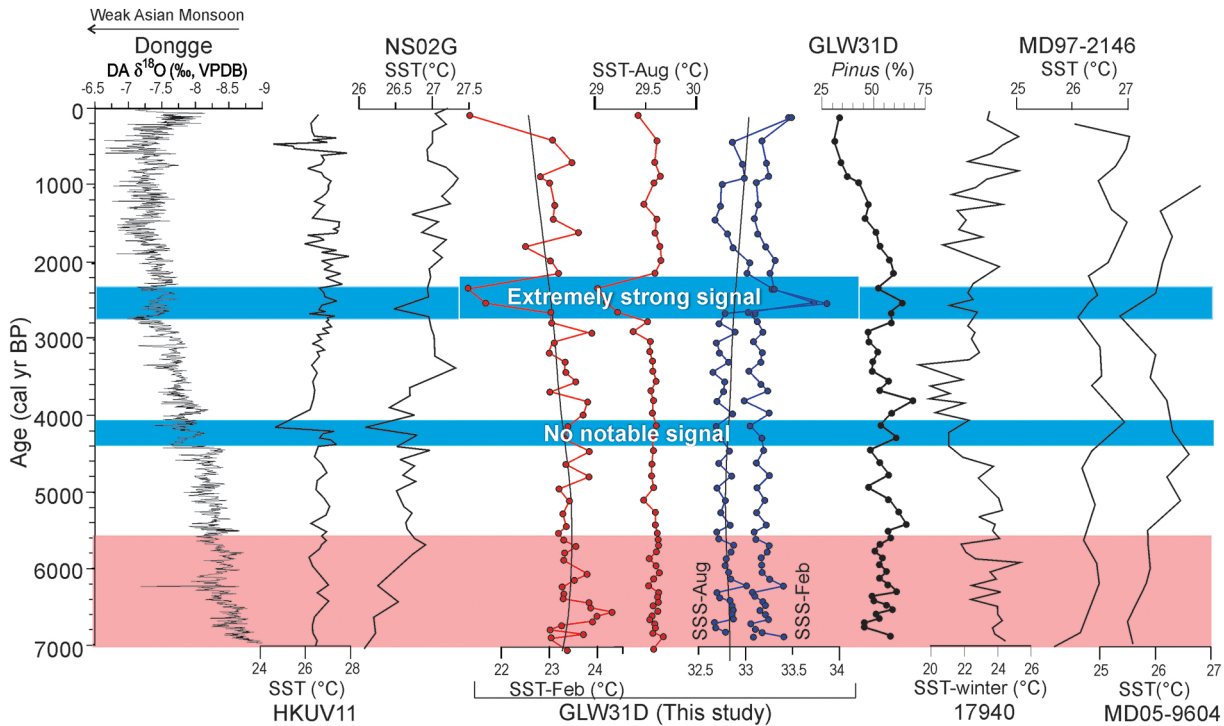


Figure 10

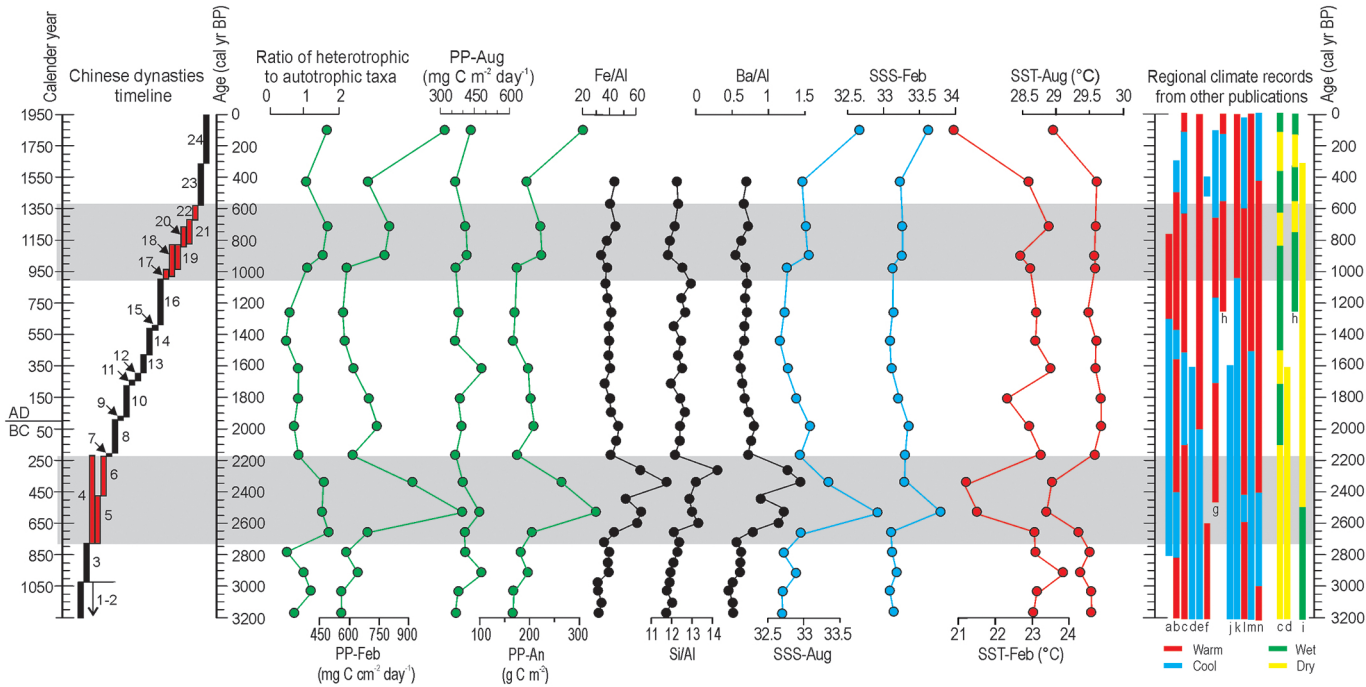


Figure 11